JGR Atmospheres

RESEARCH ARTICLE
10.1029/2019JD030384

Influence of Synoptic Pattern and Low-Level Wind Speed on Intensity and Diurnal Variations of Orographic Convection in Summer Over Pearl River Delta, South China

Xiaona Rao[1,2], Kun Zhao[1,2], Xingchao Chen[3], Anning Huang[1,2], Ming Xue[1,2], Qinghong Zhang[4], and Mingjun Wang[1,2]

[1]Key Laboratory of Mesoscale Severe Weather/MOE and School of Atmospheric Sciences, Nanjing University, Nanjing, China, [2]State Key Laboratory of Severe Weather and Joint Center for Atmospheric Radar Research of CMA/NJU, Beijing, China, [3]Department of Meteorology and Atmospheric Science, and Center for Advanced Data Assimilation and Predictability Techniques, The Pennsylvania State University, University Park, PA, USA, [4]Department of Atmospheric and Oceanic Sciences, School of Physics, Peking University, Beijing, China

Key Points:
- The spatial distributions and diurnal variations of summer convection over South China are influenced by different synoptic patterns
- Inland orographic convection is dominated by synoptic pattern with prevailing southwesterly winds within the lower troposphere
- Orographic convection is controlled by both the terrain thermal effects and the dynamic forcing with the increase of wind speed

Correspondence to:
K. Zhao,
zhaokun@nju.edu.cn

Citation:
Rao, X., Zhao, K., Chen, X., Huang, A., Xue, M., Zhang, Q., & Wang, M. (2019). Influence of synoptic pattern and low-level wind speed on intensity and diurnal variations of orographic convection in summer over Pearl River Delta, South China. *Journal of Geophysical Research: Atmospheres*, *124*, 6157–6179. https://doi.org/10.1029/2019JD030384

Received 28 JAN 2019
Accepted 10 MAY 2019
Accepted article online 29 MAY 2019
Published online 20 JUN 2019

Abstract Based on 5 years of operational Doppler radar data, the influences of atmospheric synoptic patterns and low-level prevailing wind speed on the intensity and diurnal variations of summer orographic convection occurrence frequencies over Pearl River Delta, South China, have been investigated. Results show that the inland orographic convection and rainfall generally occurs under synoptic pattern characterized with the prevailing southwesterly wind within the lower troposphere. The summer orographic convection over the mountains in northeastern Pearl River Delta is not only controlled by the orographic thermal conditions but also the dynamic forcing with the increase of wind speed. Owing to the strong windward mechanical lifting and moisture transport associated with the strong ambient onshore winds, the number of convection occurrences characterized by a dominant diurnal afternoon peak occurs much more frequently in the high-wind speed days. While due to the weak orographic mechanical lifting and moisture supply in the low-wind speed days, the number of convection occurrences in the afternoon decreases considerably and two comparable peaks occur in the afternoon and early morning. The nighttime peak in the low-wind speed days is mainly attributed to the nocturnal acceleration of the low-level southwesterly wind associated with the inertial oscillation and the corresponded enhanced windward lifting effects.

1. Introduction

As one of the three biggest population and economic zones in China, South China is also a climatological rainfall center during summer (Luo et al., 2013). Frequent heavy rainfall and associated floods bring loss of life and property damages, and urban inundation over South China almost every year (Luo et al., 2017; H. Wang et al., 2014). Based on 3 years' radar observations, X. Chen, Zhao, et al. (2014) demonstrated that convection over South China occurs most frequently along the southern coast and the windward slope of the inland northeastern mountainous area during the warm season (May–September). The spatial distribution of convection roughly matches the accumulated precipitation spatial pattern, while convective rainfall accounts for more than 45% of the total rainfall during warm season over South China (X. Chen, Zhao, et al., 2014). Recent studies have suggested that diurnal cycles of rainfall and convection over South China exhibit pronounced regional and intraseasonal variations (G. Chen et al., 2018; X. Chen, Zhao, et al., 2014; X. Chen et al., 2015; Jiang et al., 2017). Morning rainfall is dominant over offshore regions because of the surface convergence between the northerly land breeze and the prevailing southerly low-level monsoonal wind (G. Chen et al., 2018; X. Chen et al., 2016; X. Chen et al., 2015). The rainfall and convection over the inland northeastern mountainous area exhibits two diurnal peaks. The primary peak in the afternoon is associated with the solar heating effect, whereas the secondary peak during midnight to the early morning is closely related to the nocturnal acceleration of southwesterly boundary layer flow (X. Chen et al., 2015). Further studies suggested that both the background wind and moisture can influence the intensity and diurnal variations of rainfall over the coastal areas over South China (X. Chen et al., 2019; X. Chen et al., 2017; Du & Rotunno, 2018). The low-level monsoonal

wind speed is the main factor controlling the diurnal variability of monsoon convection over South China (X. Chen et al., 2017). However, few studies have conducted for the influences of low-level wind speed on the inland orographic rainfall center over Pearl River Delta (PRD), South China.

The role of large-scale wind speed on the orographic convection has been extensively investigated and revealed in previous studies. Tian and Parker (2002) investigated the orographic effects on mesoscale boundary layer convection under different wind speeds through a series of idealized 2-D numerical experiments; they found that the strong ascents and descents on both sides of the hill pose a more important impact on convection than the terrain thermal effects as the wind speed increases. Using an explicitly resolving cloud model, Miglietta and Rotunno (2009) explored the response of the along-ridge-average precipitation to the topography and the varying ambient atmosphere. Results have shown that under the conditions with relatively weaker environmental wind speed (2.5 m/s), the cold air outflow due to the convection propagates farther upstream and induces new upstream convective cells, and the stationary rainfall formation over the mountain ridge is prevented. However, for larger values of U (10, 20 m/s), the quasi-stationary convective cells and rainfall occur along the windward slope of the mountain without significant cold pool.

By using the long-term Tropical Rainfall Measuring Mission observations, Sobel et al. (2011) suggested that the diurnal cycle of precipitation over small islands is stronger over the Maritime Continent than that over the Caribbean. It is because the ambient wind over the Maritime Continent is weaker than that of the Caribbean. S. Wang and Sobel (2017) conducted idealized cloud-permitting simulations to examine the precipitating convection over small islands as a function of large-scale wind speed. Results indicated that the large-scale winds notably influence the diurnal cycles of rainfall over small tropical islands. The thermally forced sea breeze-related convection dominates when the large-scale wind is weak, whereas mechanically forced convection is pronounced when the large-scale wind is enhanced. Based on observations from the Caribbean island of Dominica, transition between thermally and mechanically forced orographic convection are studied. Smith et al. (2012) showed that precipitation over Dominica is sensitive to trade wind speed with a transition from thermally to mechanically triggered convection as the wind speed increases. Diurnally varying thermal convection is dominant and the strongest ascent occurs along the mountain ridge and the leeward side under the low wind speed conditions ($U < 5$ m/s). However, under strong trades ($U > 7$ m/s), convection driven by topography mechanically forcing occurs with the strongest updrafts over the windward slopes. By comparing observations from the Dominica Experiment field campaign with numerical simulations, Nugent et al. (2014) suggested that thermally driven convection is present with the high mountaintop surface temperature and divergence above the island under weak winds. However, topography lifting over the windward slope and leeside plunging flow are dominant under strong winds, and enhanced ventilation and cloudiness over the windward slopes reduce the mountaintop surface temperature.

Previous studies also examined the diurnal cycles of precipitation and/or convection over South China during different periods of warm season (G. Chen et al., 2009; X. Chen, Zhao, et al., 2014; X. Chen et al., 2015; Jiang et al., 2017). However, there are various weather systems even in a certain period (usually divided by month). Besides, earlier studies mainly focused on the transition from thermal forced to mechanical forced convection as the wind speed increases. However, the influences of synoptic patterns combined with wind speeds on the diurnal variation of orographic convection over PRD, South China, are still unclear and need to be deeply revealed and understood. Based on 5 years of operational Doppler radar observations at Guangzhou, China, this study first examines the spatial and temporal characteristics of summer convection over PRD, South China, under typical synoptic patterns. Then the influence of low-level ambient wind speed on the intensity and diurnal variability of inland orographic convection occurrence frequencies and related physical mechanisms are also investigated.

The rest of the paper is organized as follows: Data and methodology are introduced in section 2. Section 3 gives the results of the classification of synoptic patterns over South China. Spatial distributions and diurnal variations of the summer convection over PRD under typical synoptic patterns and different ambient wind speeds are presented in section 4. In section 5, the possible mechanisms related to the influence of low-level ambient wind speed on the orographic convection occurrence frequencies and diurnal variability are explored. Summary and conclusions are given in section 6.

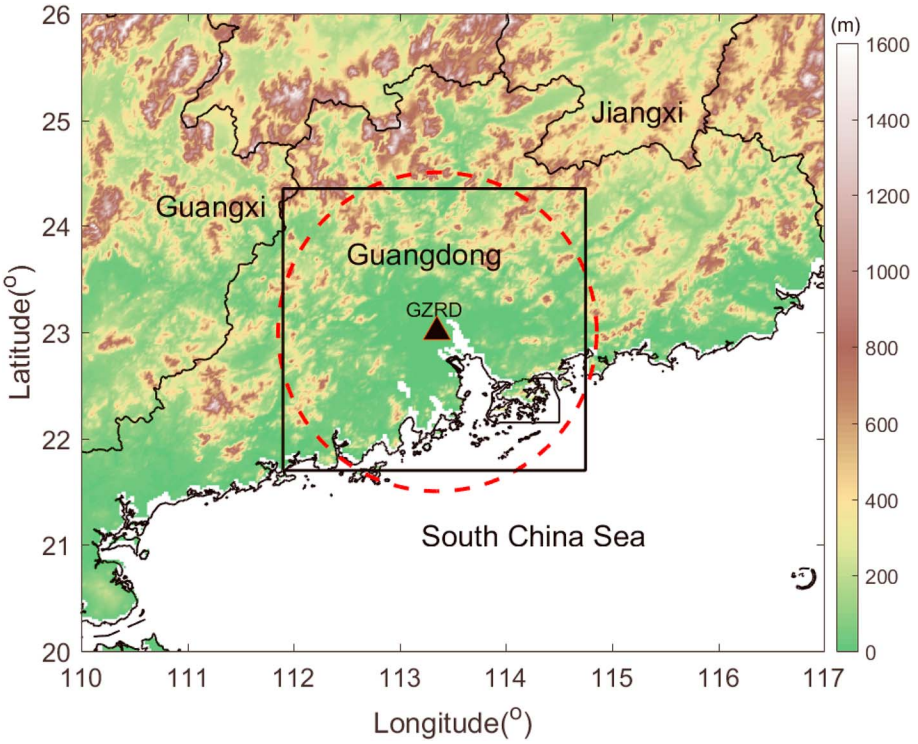

Figure 1. The location of the GZRD, together with the 150-km-range circle. The study region (Pearl River Delta) is marked by the black square (21.7–24.35°N, 111.9–114.75°E). Coastlines and provincial borders are shown by black lines. Shading denotes orography (units: m). GZRD = Guangzhou radar.

2. Data and Methodology

2.1. Radar Data and Data Processing

The radar data and processing procedure used in this study are similar to those used in X. Chen, Zhao, et al. (2014). The observed data for radar climatology were collected from China's Weather Surveillance Doppler-1998 radar at Guangzhou (GZRD in Figure 1), operated by the China Meteorological Administration (CMA). Similar to the WSR-88D radars of the United States, the S-band (10-cm wavelength) GZRD, with a 1° beam width, were operated in the VCP21 (volume coverage pattern 21) scanning mode. There are nine elevations from 0.5° to 19.5° in the VCP21 mode (Crum et al., 1993). To maintain a calibration precision of 1 dB, reflectivity of every volume scan was calibrated by using internally generated test signals. The radar reflectivity data possess a range resolution of 1 km and a 230-km maximum Doppler range. The GZRD (113.355°E, 23.0039°N) is located in the center of South China coastal region. The coverage area of the radar is characterized by a plain surrounded by mountains at moderate height (400–800 m) on the northeast and the coastline to the south. The GZRD data during each summer (June–August) of 2011–2015 are used to investigate the spatial distribution and diurnal cycle of convection over the study region of PRD (shown by black square in Figure 1), South China.

Following J. Zhang et al. (2004), the contaminated radar reflectivity caused by mountain, sea clutters, or ground was removed as well. Then the reflectivity data were bilinearly interpolated onto constant altitude plan position indicator (CAPPI) in Cartesian coordinate systems with 1-km × 1-km × 1-km resolution (Mohr & Vaughan, 1979). The CAPPIs were constructed every 6 min with horizontal coverage of 150 km × 150 km and extended up to 15 km in the vertical direction. More details on the quality control and interpolation procedures can be found in X. Chen, Zhao, et al. (2014). Following M. Chen, Wang, et al. (2014), a convection day over PRD region is defined based on the GZRD radar reflectivity ≥40 dBZ with the coverage over 16 km^2 lasting at least three times in a day.

The convective-stratiform classification scheme in Steiner et al. (1995) is applied to the GZRD 2.5-km altitude CAPPI reflectivity data. In this study, we focus on the convective components. The grid points

with a reflectivity ≥40 dBZ are defined as convective grids in the first step of the classification. And then the mean reflectivity within the 11-km radius of the convective grids defined in the first step are calculated, and grid points with reflectivity exceed the average value by a specific threshold (see Figure 7 in Steiner et al., 1995) are labeled as convective as well. Finally, the surrounding grid points within an intensity-dependent radius (see Figure 6b in Steiner et al., 1995) around each convective grid are also included as convective area. Following Romatschke et al. (2010), a convective feature refers to contiguous convective grid points at the 2.5-km height, extending vertically in each column and including all grid points from the echo base to the echo top. The number of convection occurrences (CON hereafter) is defined as the count that the grid point is covered by convective features. Based on the coverage area and echo top height, the convective features are also divided into six categories. Convective features with the coverage area larger than 400 km^2, between 100 and 400 km^2, and smaller than 100 km^2 are defined as large, medium, and small convection, respectively (Xu & Zipser, 2012). As was described in C.-Z. Zhang et al. (2006), convective features with 15-dBZ echo top height higher than 12 km, lower than 6 km are defined as deep, shallow convection, respectively. Convective features of moderate depth have echo tops between 6 and 12 km. Spatial distributions and temporal variations of convective features especially under different typical synoptic patterns and different ambient wind speeds are investigated in this study.

After identifying convective and stratiform radar echoes, different Z-R relationships are used to estimate convective and stratiform precipitation intensity at each grid, respectively. For the convective components, relationship $Z = 300\,R^{1.4}$ (X. Chen, Zhao, et al., 2014) is applied, whereas $Z = 200\,R^{1.6}$ (Marshall & Palmer, 1948) is adopted for stratiform rainfall. The total rainfall is the sum of convective and stratiform precipitation.

2.2. Synoptic Data

Data from NCEP Final (FNL, see https://rda.ucar.edu/datasets/ds083.2/) operational global analysis and National Oceanic and Atmospheric Administration Global Forecast System (GFS, see https://rda.ucar.edu/datasets/ds335.0/) are also used to conduct objective synoptic classification and investigate the large-scale environmental conditions, respectively. These reanalysis data have a horizontal resolution of 1°×1° (FNL) and 0.5°×0.5° (GFS), and both are available at 00, 06, 12, and 18 UTC each day.

2.3. Objective Synoptic Classification Method

The obliquely rotated principal component analysis (PCA) in T mode (PCT hereafter) is applied to the FNL reanalysis data to separate different synoptic patterns in this study. Compared with other synoptic classification methods, this method performs best because it is able to reproduce predefine dominant patterns embedded in the data set and the classification results contain higher temporal and spatial stability and less sensitivity to preset parameters (Huth, 1996a). This method could give more realistic and physically interpretable synoptic patterns (Compagnucci & Richman, 2008; Huth, 1996a; Huth et al., 2008). Based on the PCT method, Li et al. (2016) analyzed the long-term trends of hail day frequency in mainland China and associated changes in the atmospheric circulation patterns.

Different from commonly used PCA (S-mode PCA), PCA in T mode arranges input data matrix for PCA process in a different way so that the columns of input matrix represent time observations while the rows refer to grid points. In order to attain more realistic and physically interpretable synoptic patterns, an oblique rotation based on Richman (1986) is applied to a few retained leading components after the PCA process. Finally, each day pattern is classified to the type for which it has the highest loading. The method is developed by an open source software package called cost733class within the framework of COST Action 733 "Harmonisation and Applications of Weather Type Classifications for European Regions" (Philipp et al., 2016). More details about this method can refer to Huth (1996a, 1996b).

2.4. Harmonic Analysis

To reveal the diurnal variations of CON, the 24-hr time series of CON are normalized by their daily mean according to $N(h) = \frac{CON(h) - CON_m}{CON_s}$, where h ranging from 0 to 23 indicates the local standard time (LST hereafter, LST = UTC + 8). $CON_m = \frac{1}{24}\sum_{h=0}^{h=23} CON(h)$ refers to the daily mean of CON, and

$CON_s = \sqrt{\frac{1}{24}\sum_{h=0}^{h=23}(CON(h)-CON_m)^2}$ is the standard deviation of CON. Then harmonic analysis (Dai, 2001; Wallace, 1975; Wu et al., 2018; Yin et al., 2009) is applied to the normalized 24-hr time series of CON data to obtain the amplitudes and phases of convection diurnal and semidiurnal cycles. The first two harmonic components are retained to represent the diurnal and semidiurnal cycles:

$$f(t) = \bar{f} + S_1(t) + S_2(t) + \text{residual}, \tag{1}$$

$$S_m(t) = C_m \times \cos\left(m\frac{2\pi}{24}t - \sigma_m\right), \tag{2}$$

$$e_m = \frac{0.5C_m^2}{f_{\text{var}}}, \tag{3}$$

$$F_m = \frac{0.5C_m^2 \times (24-2-1)}{(f_{\text{var}} - C_m^2)\times 2}, \tag{4}$$

where $m = 1, 2$ denotes the first (S_1) and second (S_2) harmonics and represent the diurnal and semidiurnal harmonic, respectively. The higher-order harmonics of the variability of CON are included in the last term (residual) of equation (1); $\bar{f}$ is the daily mean value of CON. The $t = 1,2,3, \ldots ,24$ represents each hour of a day ranging from 0000 to 2300 LST and $f(t)$ is the estimation of CON at each hour of a day. C_m and σ_m represent the amplitude and the phase of the mth harmonic component, respectively; f_{var} is the total daily variance of CON values; e_m, defined as the percentage of total diurnal variations explained by the mth harmonic, is an index to evaluate the contribution of the mth harmonic to total daily variance. Results show that S_1 and S_2 can explain up to 90% of the total variance (see section 4.3), so the error induced by neglecting those higher-order harmonics in equation (1) should be small. F_m can be calculated according to the definition in equation (4). By comparing F_m with the inverse of the F distribution function with 2 and 21 degrees of freedom at significance level 0.9, the F test is carried out to examine the significance of the harmonics (Benedetto, 1996; Wu et al., 2018; Yin et al., 2009).

The diurnal variations (diurnal and semidiurnal cycles) described by the first two harmonics under different wind speeds are then examined to investigate the wind speed's influence on the diurnal variations of the orographic convection.

3. Synoptic Patterns

A summary of an objective classification of synoptic patterns during summer from 2011 to 2015 (460 days in total) is presented in this section. The spatial patterns of geopotential height at 925 hPa over South China (13–33°N, 107–132°E) are classified into nine types (named from types 1 to 9) using the PCT method. The nine synoptic patterns are ranked according to their occurrence frequencies during the whole summer.

The corresponding geopotential heights and mean horizontal wind vectors at 925 hPa for each synoptic pattern are shown in Figure 2. More than 65% of the 460 days for the nine synoptic patterns is contributed by the typical synoptic patterns of types 1 and 2 with the prevailing southerly monsoon flow in PRD (the black box in each graph). The most frequent occurrences of type 1 (226 days, 49.1%) with the prevailing southwesterly monsoon flow in PRD dominate the whole summer season with the highest occurrence frequencies in June. This southwesterly wind is closely related to the high pressure gradient between the Western Pacific subtropical high located around 23°N and the monsoon trough located over Indochina (not shown). The Western Pacific subtropical high moves northward to 28°N, while a low-pressure center is located between Vietnam and Hainan Island in the type 2 pattern. The axis of the pressure gradient shifted in a northeast-southwest direction, resulting in a stronger southeasterly flow over the PRD. The occurrence frequencies for the other seven patterns (types 3–9) are much smaller than those of types 1 and 2. In the types 3–9, the PRD is not under the influence of the prevailing southerly monsoonal winds, so we only focus on the cases with the synoptic patterns of types 1 and 2 in this study.

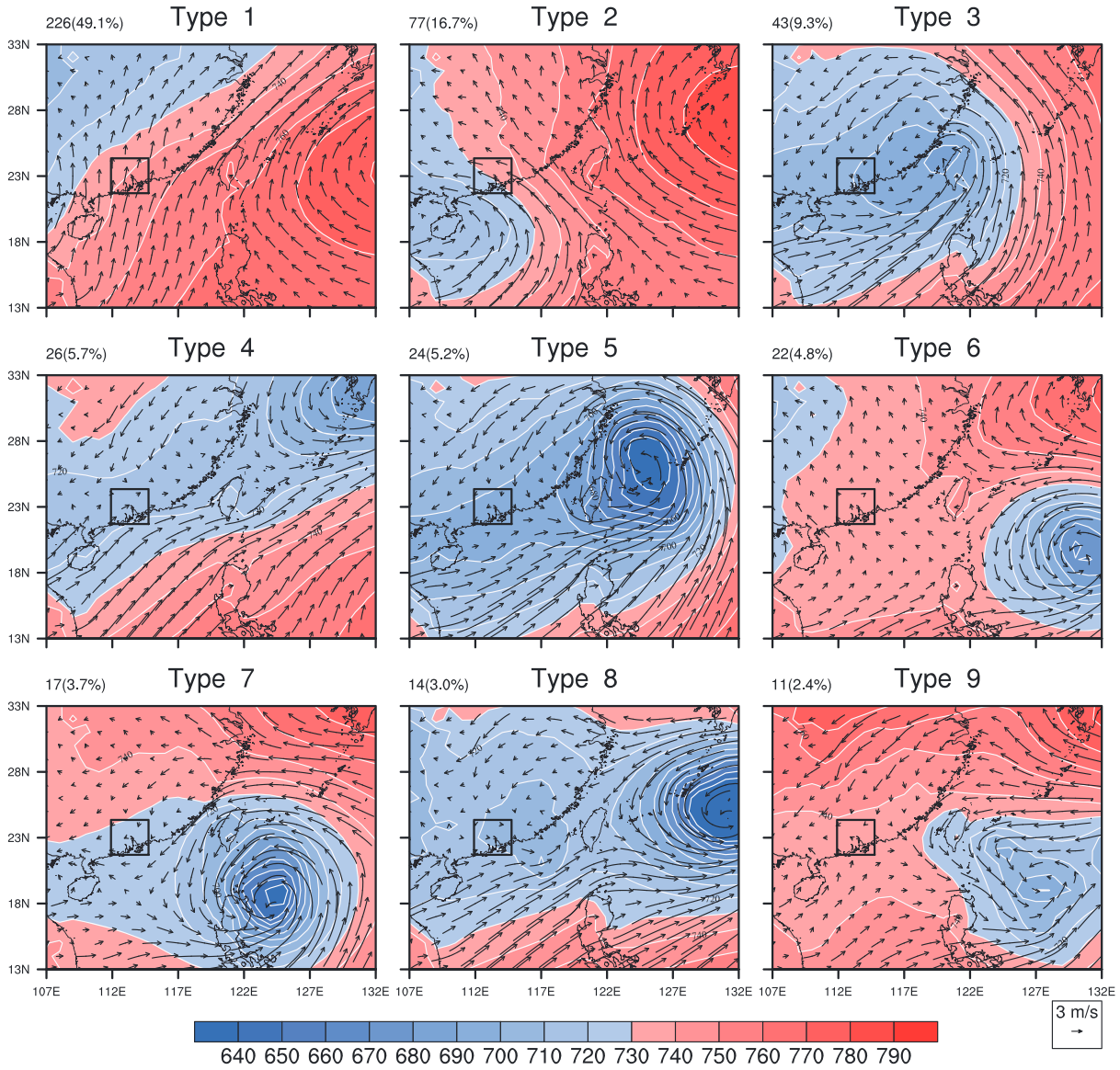

Figure 2. The nine synoptic patterns (types 1–9) based on geopotential height at 925 hPa (shading, units: gpm) over South China in summer during 2011–2015. The number of days for each pattern and their percentages are shown in the top left; the mean horizontal wind vectors at 925 hPa are superimposed; black boxes represent Pearl River Delta region.

Based on the definition of convection day in section 2.1, 381 days and 187 (71) days are identified as convection days for the whole summer and type 1 (type 2) pattern, respectively. Analysis of convection spatial distribution and diurnal variations follows are based on the convection days.

4. Spatial and Diurnal Variations of Convection Over Pearl River Delta

4.1. Spatial Distributions and Diurnal Variations of the Convective Features and Rainfall in Typical Synoptic Patterns

From the radar climatology perspective, X. Chen, Zhao, et al. (2014) showed that the southern coast and the windward slope of the northeastern mountainous area over South China are the two hotspots of convective features during May to September. Figure 3a shows the spatial distribution of the accumulated CON in summer during 2011–2015. The accumulated CON at each grid point is counted as the total number of times that the grid point is recognized as convective grid within the five summer seasons. By extending the radar

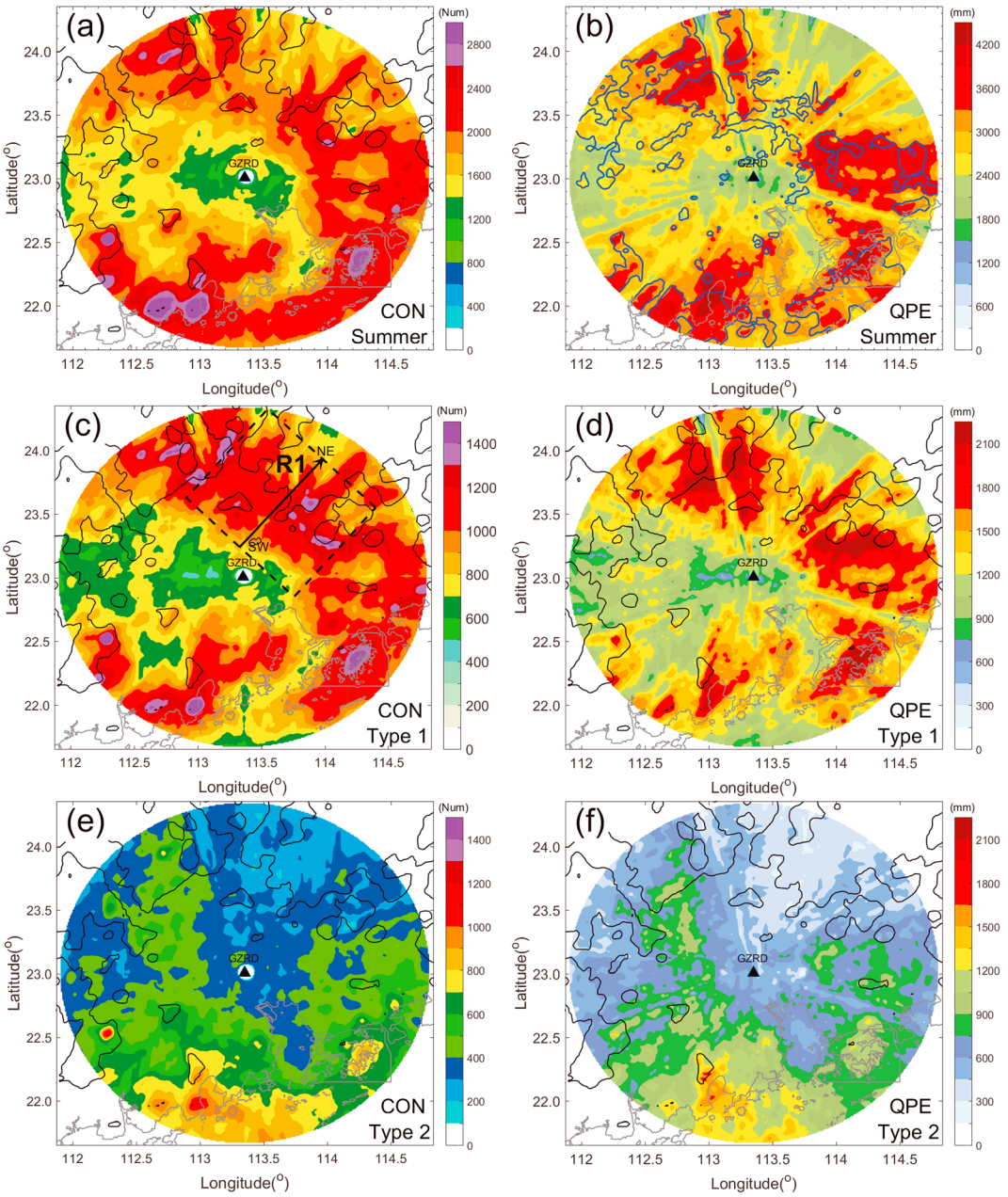

Figure 3. (left) Spatial distributions of accumulated number of CON (units: Num), (a) during 2011–2015 summer seasons, (c) under the synoptic pattern of type 1 and (e) under the synoptic pattern of type 2. (b, d, f) As in (a, c, e) but for accumulated total rainfall based on radar (QPE, units: mm). Black contours indicate orography of 150 m. Blue contours in (b) represent the percentage of convective rainfall to 5-year total rainfall during the whole summer at 80%. Note that the range of color bar in (a) or (b) is different from that in (c, e) or (d, f). CON = number of convection occurrences; ZRD = Guangzhou radar; QPE = quantitative precipitation estimate.

observation from 3 to 5 years (2011–2015), we find that the convective features occur most frequently along the southern coast and the northeastern inland mountainous region during summer, which is consistent with findings of X. Chen, Zhao, et al. (2014). The spatial pattern of accumulated total rainfall based on the radar quantitative precipitation estimate using the *Z-R* relationships is shown in Figure 3b. The accumulated rainfall at each grid point is the sum of hourly rainfall during five summer seasons. Similar to CON distribution, the northeastern inland mountainous area and south coast are two hotspots of summer rainfall, and convective rainfall contributes about 80% of total rainfall.

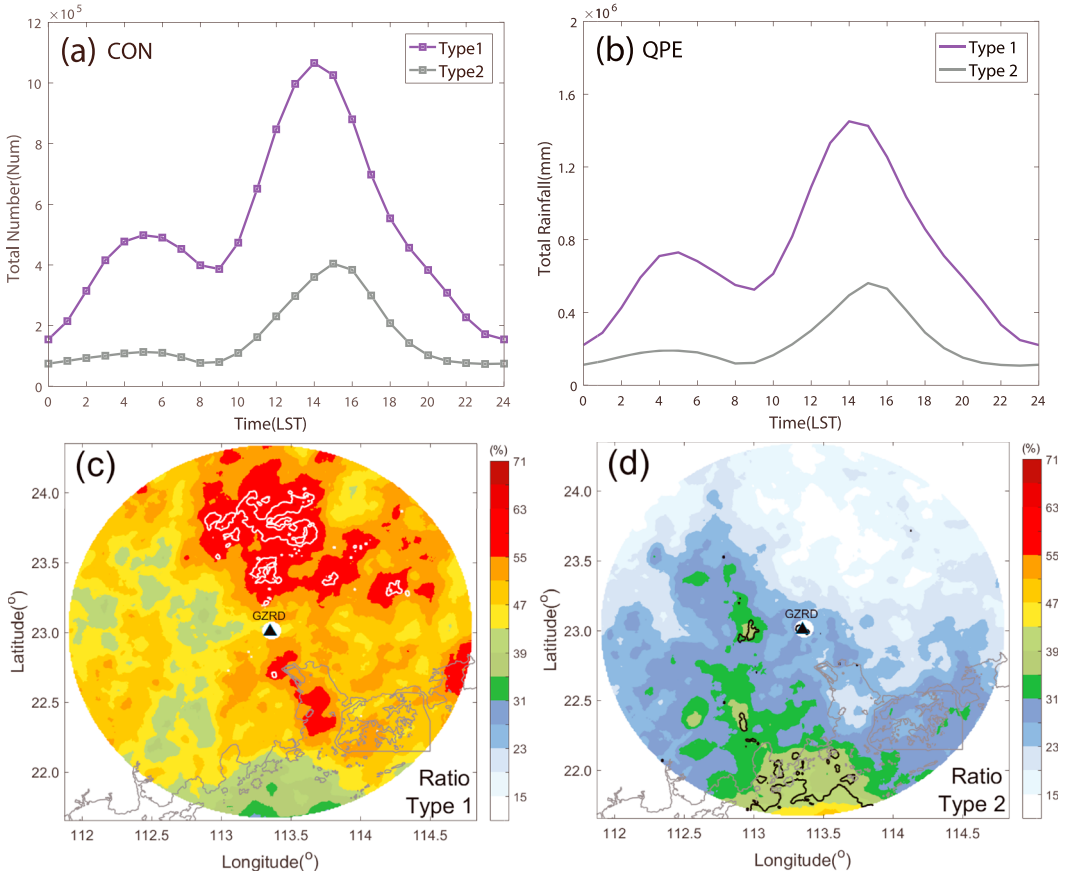

Figure 4. Diurnal cycles of (a) total number of CON (units: Num), (b) accumulated total rainfall (QPE, units: mm) over inland mountainous region (indicated by R1 box in Figure 3c) for types 1 and 2. (c) Percentage of type 1 to the whole summer in total number of convection occurrences (shading, units: %) and total rainfall (white contours: 60%). (d) As in (c) but for type 2; the black contours are 40%. CON = number of convection occurrences; GZRD = Guangzhou radar; QPE = quantitative precipitation estimate.

Figures 3c and 3e show the spatial distributions of the five summers' accumulated CON corresponding to the synoptic patterns of types 1 and 2, respectively. The CON corresponding to the synoptic pattern of type 1 exhibits two maximal centers with one located along the southern coast and the other situated at the windward slope (low-level prevailing winds are close to southwesterly and approximately perpendicular to the northeastern mountain ridges in type 1) of the inland mountainous area in northeastern PRD (R1 box in Figure 3c). The spatial distribution of CON in type 1 (Figure 3c) are similar to the spatial pattern of total CON in summer (Figure 3a). CON in the windward slope of northeastern mountains is higher than that in the south coast area under the synoptic pattern of type 1, while the south coastal area undergoes more convection during the whole summer. It is probably because the low-level prevailing wind direction over South China is almost southwesterly and roughly perpendicular to the northeastern mountain ridges under the synoptic pattern of type 1, resulting in much stronger orographic mechanical lifting effect than that of the whole summer with southerly winds as an average. The convection corresponding to the type 2 synoptic pattern occurs more frequently along the coast (Figure 3e). The spatial distributions of total rainfall under synoptic pattern of types 1 and 2 (Figures 3d and 3f) approximately match those of CON. Precipitation is mainly concentrated on the northeastern inland mountainous area and south coast (south coast) in synoptic pattern of type 1 (type 2). Therefore, the spatial distributions of CON and rainfall over PRD are closely related to the synoptic patterns. More than 60% of the total convection and rainfall in summer over the northeastern mountainous area is contributed by those corresponding to the type 1 synoptic pattern (Figure 4c). However, type 2 synoptic pattern contributes more than 40% (less than 15%) of convection and rainfall over offshore region (inland northeastern mountainous region; Figure 4d). So type 1 is the dominant synoptic pattern in terms of the orographic summer convection (and rainfall) over northeastern PRD.

The prevailing warm and moist low-level southerly flows over South China lead to a low free convection level (X. Chen, Zhao, et al., 2014). Therefore, the orographic lifting effect is strong enough to trigger convection on the windward slope. Various studies have indicated that the characteristics and physical mechanisms of coastal enhanced rainfall and convection are closely related to the surface friction and land-sea breeze (G. Chen et al., 2018; X. Chen et al., 2017; X. Chen et al., 2015; Jiang et al., 2017).

Diurnal variation is an important basic feature of convection and rainfall. During the past decade, diurnal cycles of convection and rainfall over South China have been extensively studied through rain gauge, radar, and satellite data (G. Chen et al., 2018; G. Chen et al., 2013; X. Chen, Zhao, et al., 2014; X. Chen et al., 2015; Luo et al., 2013; Xu & Zipser, 2011; Yuan et al., 2010; Zhou et al., 2008). Results showed that the diurnal features of rainfall and convection exhibit strong regional and intraseasonal variability. The diurnal variations of convection over the inland mountainous over South China are closely related to the diurnal variations of the summer monsoonal wind. The diurnal variations of the inland orographic convection under the typical synoptic pattern of types 1 and 2 are examined below.

Figure 4a shows the diurnal variations of total CON (units: Num) accumulated at all grids along the inland mountainous windward slope (R1 box in Figure 3c) under the synoptic patterns of types 1 and 2. Diurnal cycles of total rainfall over inland mountainous area in types 1 and 2 are presented in Figure 4b. The CON and precipitation on the windward slope corresponding to the type 1 synoptic pattern exhibit two diurnal peaks, with the primary peak in the early afternoon around 1400 LST and the secondary peak in early morning (0400–0500 LST). Compared with the situations corresponding to the type 1 synoptic pattern, the diurnal cycle of CON and rainfall with the type 2 synoptic pattern show a slightly delayed afternoon peak (around 1500–1600 LST) and a much weaker morning peak (around 0500–0600 LST). The pronounced afternoon peak is apparently related to the increases of local instability due to the diurnal solar heating (Luo et al., 2013). X. Chen et al. (2015) also noted the secondary diurnal peak in the early morning over the windward slope of northeastern mountains during Mei-Yu season, which is likely due to the nocturnal acceleration and enhanced lifting on the windward slope of southwesterly boundary layer flow.

In summary, the spatial distributions and diurnal cycles of precipitation under different synoptic patterns basically match those of convection occurrences. In addition, the diurnal cycle of convection shown in the current study is consistent with the rainfall diurnal cycles revealed by the long-term satellite observations (X. Chen et al., 2019). Therefore, we only focus on characteristics of convection occurrences under type 1 synoptic pattern in following sections.

4.2. Spatial Distributions of Convective Features Under Different Wind Speeds in Dominant Synoptic Pattern

As mentioned earlier, X. Chen et al. (2017) showed that the low-level monsoonal wind speed is a key factor influencing the diurnal variations of the rainfall over the coastal regions of South China in Mei-Yu season. However, the influence of the monsoonal wind speed on the diurnal variations of inland orographic convection remains unclear. In this section, we examine the spatial distributions and diurnal cycles of the summer convection over the inland mountainous region under different low-level prevailing wind speeds in the dominant type 1 synoptic pattern, which accounts for the most inland orographic convection during summer.

For the type 1 synoptic pattern, the prevailing wind in the lower troposphere is close to southwesterly on average. To investigate the impact of the wind speed on the diurnal cycles of convection, we calculate the daily mean prevailing wind speed at 925 hPa over PRD region (21.7–24.35°N, 111.9–114.75°E; the black square in Figure 1) for each convection day (total number of 187 days) with the type 1 synoptic pattern based on the 0.5° × 0.5° GFS data. Then all the 187 days are sorted according to the mean wind speed at 925 hPa. Finally, 30% days corresponding to the type 1 pattern with relatively stronger wind speeds higher than 6.5 m/s (weaker wind speeds lower than 4.5 m/s) are defined as the high (low)-wind speed days, while the rest of (40%) days with wind speeds ranging from 4.5 to 6.5 m/s are considered as the moderate-wind speed days. Fifty-six high-wind speed days, 56 low-wind speed days, and 75 moderate-wind speed days are picked out for composite analysis of different wind speed ranges.

Figure 5d displays the monthly variation of the days with different wind speeds in summer. The high-wind speed and the moderate-wind speed days occur more frequently in June and July, while relatively more low-wind speed days appear in August. Figures 5a–5c show the spatial distribution of the daily mean CON under

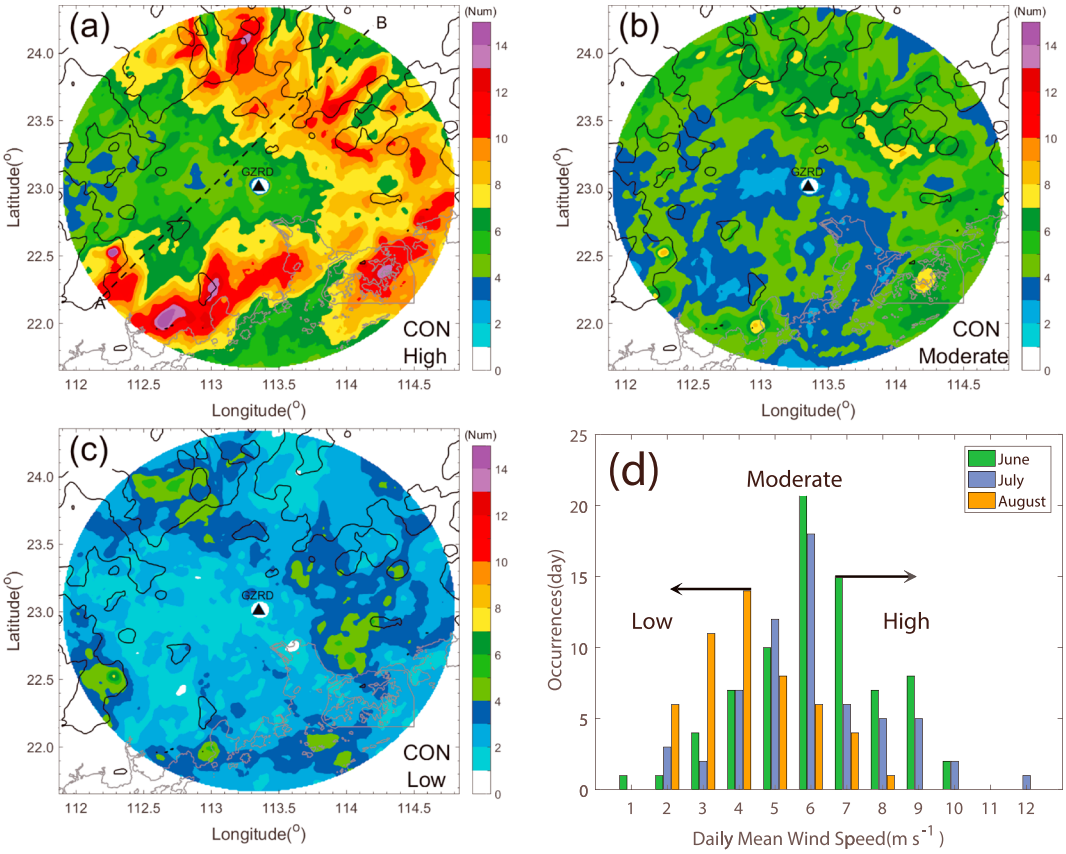

Figure 5. Spatial distributions of daily mean number of CON (units: Num) in (a) the high-wind speed days, (b) the moderate-wind speed days, and (c) the low-wind speed days. Black contours indicate orography of 150 m. (d) Monthly variation in occurrence days of different wind speeds in type 1. All daily mean wind speeds in type 1 are divided into 12 intervals ranging from 0.5–1.5 to 11.5–12.5 m/s. CON = number of convection occurrences; GZRD = Guangzhou radar; QPE = quantitative precipitation estimate.

the high-wind speed, the moderate-wind speed, and the low-wind speed days, respectively. (For example, the daily mean CON in the high-wind speed days is defined as the accumulated CON of the high-wind speed days at each grid divided by 56 days.) It is clearly shown that the intensity and spatial pattern of daily mean CON vary with the ambient low-level wind speed. Convection occurs most frequently during the high-wind speed days, and it exhibits two maximal centers with one situated along the south coast (mean CON > 12) and the other located on the windward slope of the northeastern mountains (mean CON ~9). CON decreases to less than 5 along the coast in the moderate-wind speed days, and the inland mountain area experiences a relatively smaller decrease. CON along the south coast and on the windward slope of the northeastern mountains is significantly reduced to less than 4 in the low-wind speed days. The south coastal convection over South China reduced as the ambient wind speed decreases, consistent with previous studies (X. Chen et al., 2017; X. Chen, Zhao, et al., 2014). At the high onshore wind speed, the coastal rainfall/convection is closely related to the strong low-level convergence induced by the differential surface friction and the small hills at the coast (X. Chen et al., 2017). However, the influence of wind speed on the diurnal variations of northeastern orographic convection and associated mechanisms are still unclear and will be analyzed in the below sections.

4.3. Diurnal Cycle and Propagation of Convection in Different Wind Speeds Days of the Dominant Synoptic Pattern

The diurnal variations of 24-hr time series' daily mean CON over the inland mountainous windward slope (box R1 in Figure 3c) in different wind speeds days of type 1 synoptic pattern are presented in Figure 6a. Diurnal cycle of daily mean CON exhibits a dominant early afternoon peak (around 1300–1400 LST) and a local maximum in the early morning around 0400–0600 LST in the high-wind speed days. In the

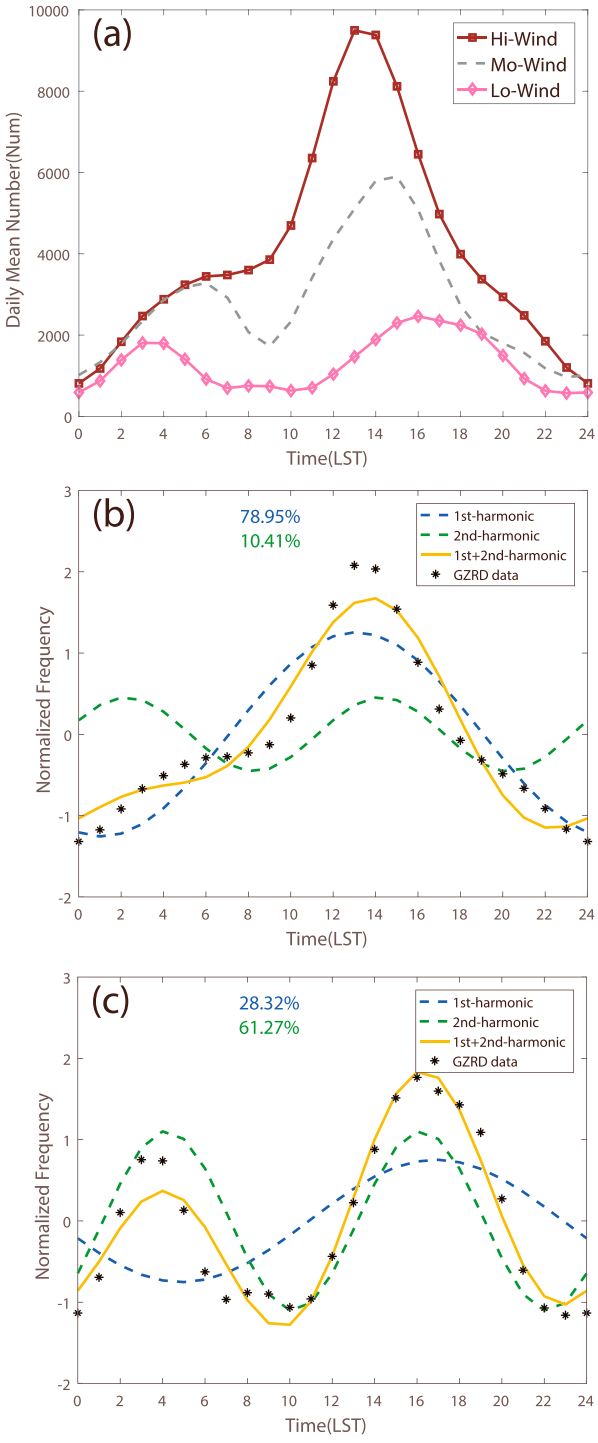

Figure 6. (a) Diurnal cycles of daily mean number of convection occurrences over inland northeastern mountainous slope (R1 box in Figure 3c; units: Num) under different wind speeds days in type 1. Observed normalized hourly mean number of convection occurrences (dots) together with the fitted first (dashed blue curve), second (dashed green curve) harmonics, and the sum of the two harmonics (yellow curve) in (b) the high-wind speed days and (c) the low-wind speed days in type 1.The percentages denoted by blue and green numbers represent the explain variance of the first and second harmonic, respectively. LST = local standard time; GZRD = Guangzhou radar.

moderate-wind speed days, the CON shows two diurnal peaks with a primary peak in the early afternoon (around 1400–1500 LST) and a secondary one in the early morning (around 0500–0600 LST). Compared with the moderate-wind speed days, the afternoon peak appears relatively later (1600–1700 LST) while the morning peak occurs slightly earlier (0300–0400 LST) under the low-wind speed conditions. In addition, the amplitude of afternoon peak is much weaker, resulting in two comparable diurnal peaks in the low-wind speed days. CON in the afternoon decreases with declining wind speed. In particular, the CON maximum in the afternoon under the high-wind speed conditions is nearly 5 times of that under the low-wind speed conditions. We compare the differences in the CON between the high-wind speed and the low-wind speed days in the following sections to reveal the influence of wind speed on the diurnal variation and intensity of the inland orographic convection occurrence frequencies.

To further quantify the differences in the CON diurnal variation between the high-wind speed and the low-wind speed days, we adopt the harmonic analysis on the normalized 24-hr time series of the CON regionally averaged over the inland mountainous area for the high-wind speed and the low-wind speed days. The results of the harmonic analysis are shown in Figures 6b and 6c. The percentage of the variances explained by the diurnal harmonic (S_1) and semidiurnal harmonic (S_2) to the total variance are indicated by the blue number and the green number, respectively. It shows that the sum of explained variance for the first two harmonics reaches nearly 90% for both the high-wind speed and the low-wind speed days, suggesting that the sum (yellow line in Figures 6b and 6c) of the first two harmonics explain the majority of the daily variance. Differences can also be found for the CON diurnal variations with different wind speeds. The first harmonic explains much more variance than the second one (79% vs. 10.4%) in the high-wind speed days. Only the first one reaches the 90% significance level for the F test. In the low-wind speed days, the explained variance of the semidiurnal harmonic is much larger than the diurnal one (61.3% vs. 28.3%), and both harmonics are significant, indicating that the CON corresponding to the high (low)-wind speed days exhibits single afternoon peak (two comparable morning and afternoon peaks).

All convective features under the high-wind speed and the low-wind speed conditions are also divided into six categories according to the definition described in section 2.1. The diurnal cycles of convective features with different sizes and vertical depths over the windward slope of inland mountains (R1 box in Figure 3c) under different wind speeds conditions are also compared in Figure 7. The convective features are mainly contributed by large (and/or deep and moderate depth) convective features in the high-wind speed days. In the low-wind speed days, the morning convection is mainly contributed by large (and/or deep) convective features. In the afternoon, however, the occurrences of the convective features with large and medium size (and/or with deep and moderate depth) are comparable, indicating that smaller convection is more likely to occur in the afternoon under low-wind speed conditions. In addition, the diurnal cycle of occurrences of convective features varies with size and vertical depth. Large and deep convection occurrences exhibit two diurnal peaks with the primary one in the early afternoon and the secondary peak in the early morning both under the high-wind speed and the low-wind speed conditions (solid red lines). As for convective features with medium size and moderate vertical depth, there is only a dominant afternoon peak

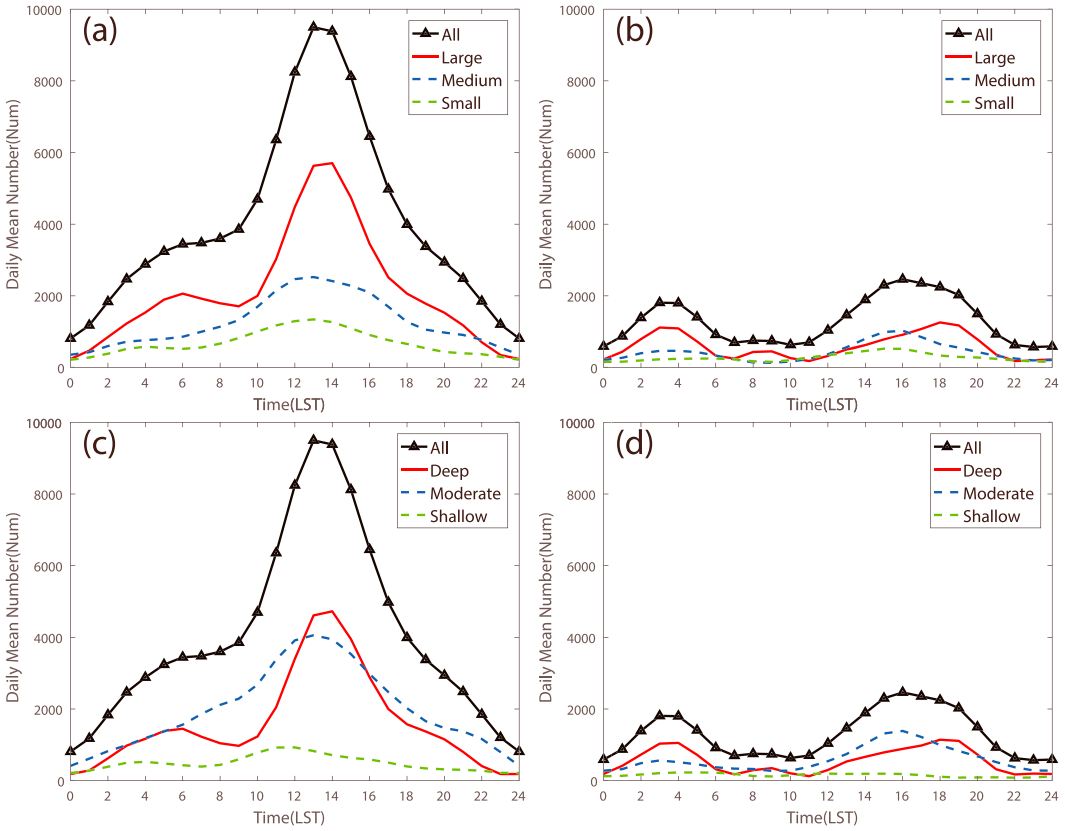

Figure 7. Diurnal variations of the convective features occurrence number over the inland northeastern mountainous region (R1 box in Figure 3c). Convective features with different sizes in (a) the high-wind speed days and (b) the low-wind speed days and for convective features with different depths in (c) the high-wind speed days and (d) the low-wind speed days. LST = local standard time.

(dashed blue lines). In general, small-scale convective activities are closely related to the afternoon solar heating effects and the corresponding upward branch of mountain-plains solenoid. However, larger convective systems are induced by both this afternoon thermal forced circulation and an enhanced orographic lifting induced by the nocturnal enhancement of the low-level wind speed. As a result, the diurnal cycle of larger convective systems shows a double peak pattern (Figure 7). The detailed physical mechanisms will be discussed in section 5.

Spatial propagation is also another important characteristic of convection, daily Hovmöller diagrams of the hourly averaged CON in the high-wind speed and the low-wind speed days are shown in Figures 8a and 8b, respectively. These two Hovmöller diagrams are aligned along the short dimension (black SW-NE arrow in Figure 3c, approximately from southwest to northeast orientation) and averaged along the long direction (perpendicular to SW-NE arrow) of the R1 box in Figure 3c. In the high-wind speed days, one dominant maximum can be seen in the early afternoon (around 1200–1500 LST). Similar to the results of Miglietta and Rotunno (2009), the high-CON region in the high-wind speed days is quasi-stationary and can be found mainly over the mountainous and windward regions. This convection hotspot in the afternoon is related to the solar heating, which is more effective in triggering convection over the mountain slope area when the mountainous elevated heating is favorable for the formation of upslope solenoidal circulations (X. Chen et al., 2015).

In the low-wind speed days, the CON exhibits two comparable diurnal peaks with one in the early morning around 0300–0500 LST and the other in the afternoon around 1400–1700 LST (Figure 8b). The high-CON centers are located over the mountain region and the adjacent plains (see the terrain contour in the bottom of Figures 8a and 8b). The early morning convection propagates from the mountainous area to the upstream lower plains area, with a propagating speed about 6 m/s. This upstream propagation may be related to the

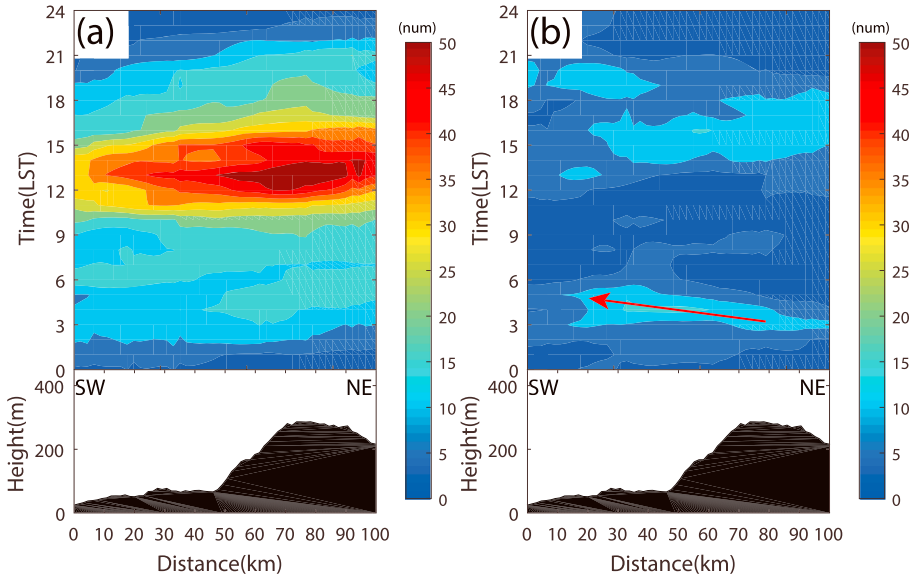

Figure 8. Hovmöller diagrams of mean hourly number of convection occurrences in (a) the high-wind speed days and (b) the low-wind speed days along direction SW-NE arrow and averaged along the other direction (perpendicular to SW-NE arrow) of the R1 box in Figure 3c. Black contour at the bottom of each panel represents the mean orography along SW-NE arrow. LST = local standard time.

cold air outflow propagating upstream (Miglietta & Rotunno, 2009). Dynamical pressure perturbations induced by low-level wind maxima (C. C. Wang et al., 2015) as well as the thermally driven gravity waves (Du & Rotunno, 2015, 2018) are also two possible mechanisms, and additional analyses are necessary in the future.

5. Possible Mechanisms Related to the Intensity and Diurnal Cycle of Orographic Convection in Different Wind Speed Days of the Dominant Synoptic Pattern

Based on the GFS reanalysis data, the atmospheric thermodynamic and moisture conditions under different low-level wind speeds of type 1 synoptic pattern are analyzed in this section. The possible mechanisms responsible for the influences of low-level wind speed on the inland orographic convection are also discussed.

5.1. Thermal Environment Conditions

Mean surface temperature and wind fields of 925 hPa at 1400 and 0200 LST are shown in Figure 9 for the high-wind speed (Figures 9a and 9c) and the low-wind speed days (Figures 9b and 9d). Large diurnal variation of surface temperature mainly exists over land. However, the temperature diurnal ranges over the ocean are relatively weaker due to much larger heat capacity of ocean relative to land. In addition, in the high-wind speed days, the mean temperature at 1400 LST over land in PRD is 3–4 K lower than that in the low-wind speed days, which is likely related to enhanced ventilation and cloud shading effects (Nugent et al., 2014). Consequently, the land sea thermal contrast in the afternoon is much stronger during the low-wind speed days than that during the high-wind speed days. The diurnal variations of thermally forced winds induced by the land sea contrast are stronger and consequently harder to be reversed (X. Chen et al., 2017) in the low-wind speed days. As a result, the establishment time of the sea (or land) breeze is earlier in the high-wind speed days than that in the low-wind speed days.

Figures 10 and 11 show the spatial distributions of convection inhibition energy (CIN) and convection available potential energy (CAPE) at 1400 LST and 0200 LST under different wind speeds and the differences between the high-wind speed and low-wind speed days. It is clearly noted that the CIN over the northeastern mountains does not show obvious differences between the high-wind speed and the low-wind speed days at 1400 LST (Figure 10e). While CIN in the low-wind speed days is larger than that in the high-wind speed days

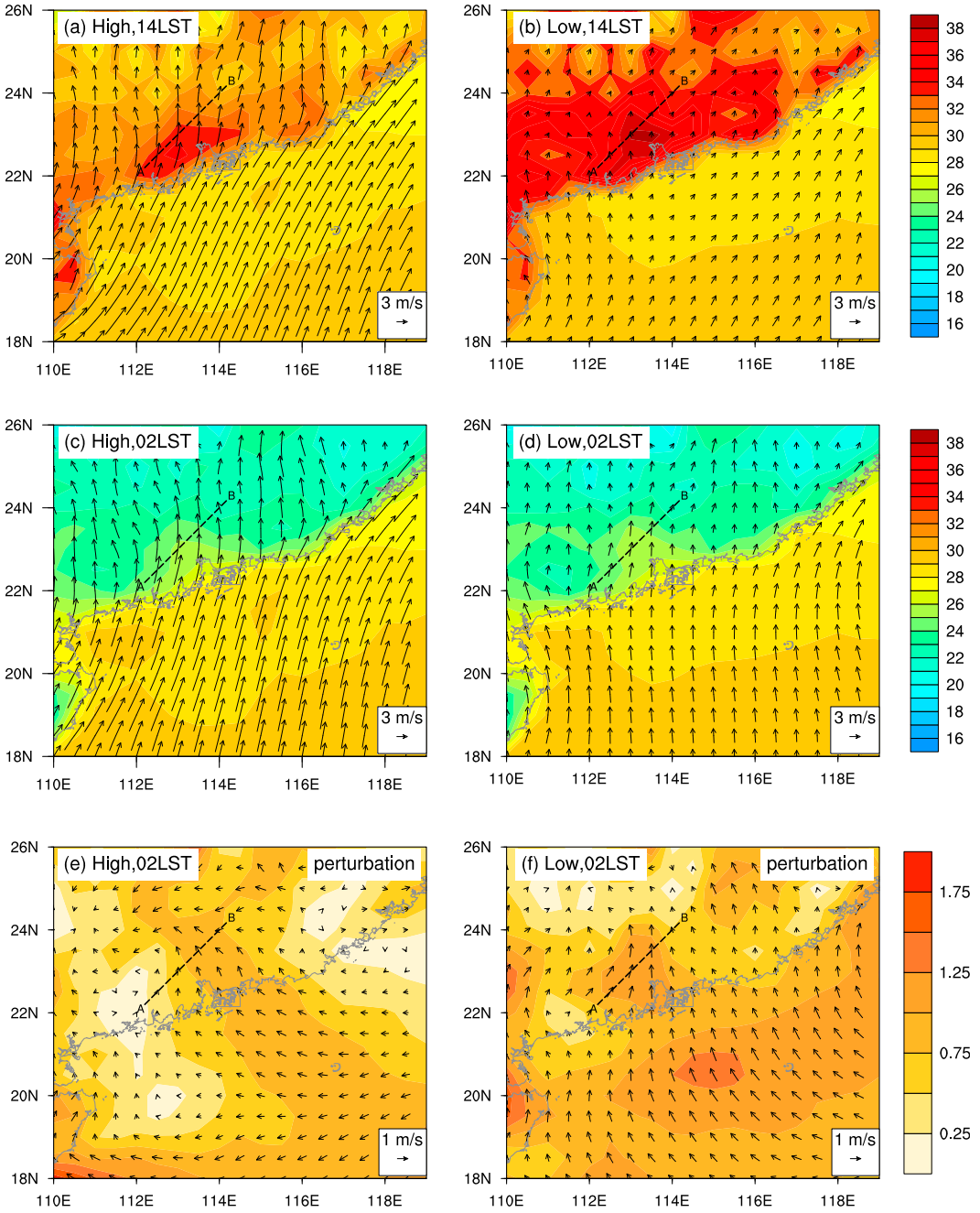

Figure 9. Mean surface temperature (shading, units: °C) and mean horizontal wind vectors (arrows) at 925 hPa at (a) 1400 LST and (c) 0200 LST and (e) perturbation wind vectors (arrows) and speeds (shading, units: m/s) at 0200 LST in the high-wind speed days. (b, d, f) As in (a, c, e) but for the low-wind speed days. Dashed lines A-B indicate the line A-B in Figure 5a. LST = local standard time.

at 0200 LST (Figure 10f), which is associated with smaller CON in the morning under the low-wind speed conditions (Figure 6a). In addition, the CAPE over the northeastern mountainous area in the high-wind speed days is slightly smaller than that in the low-wind speed days both at 1400 LST and 0200 LST (Figure 11). The less CAPE over R1 region at 1400 LST in the high-wind speed days is very likely because it was during or after the intense convective activity which occurs around 1100–1500 LST (Figure 8a). However, even after 1400 LST, the CON is still higher in the high-wind speed days. This suggests that the topography mechanical lifting effect should be an important contributor as the ambient wind speed increases (Smith et al., 2012; S. Wang & Sobel, 2017).

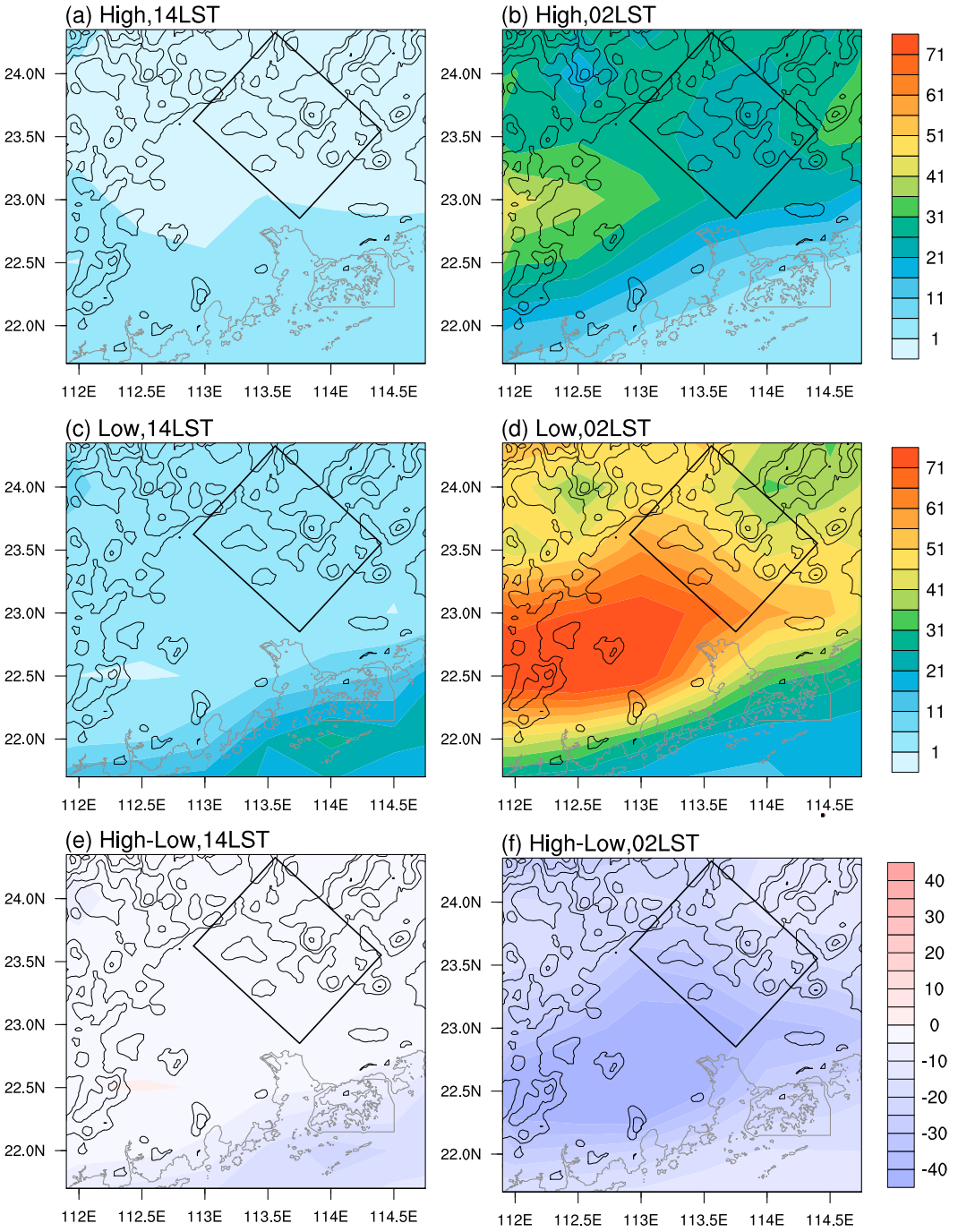

Figure 10. Mean surface CIN (units: J/kg) over Pearl River Delta region in the high-wind speed days at (a) 1400 LST, (b) 0200 LST, and in the low-wind speed days at (c) 1400 LST and (d) 0200 LST; CIN of the high-wind speed days minus the low-wind speed days at (e) 1400 LST and (f) 0200 LST. To facilitate comparison, CIN is multiplied by −1. Black boxes corresponding to R1 box in Figure 3c represent the windward slope of northeastern mountainous region. Black contours, from 100 to 1,100 with 200-m intervals, indicate orography. CIN = convection inhibition energy; LST = local standard time.

5.2. Diurnal Variations of Low-Level Environmental Flow

Diurnal variations of environmental flows and associated impacts on the inland orographic convection under the high-wind speed and low-wind speed days are discussed in this section.

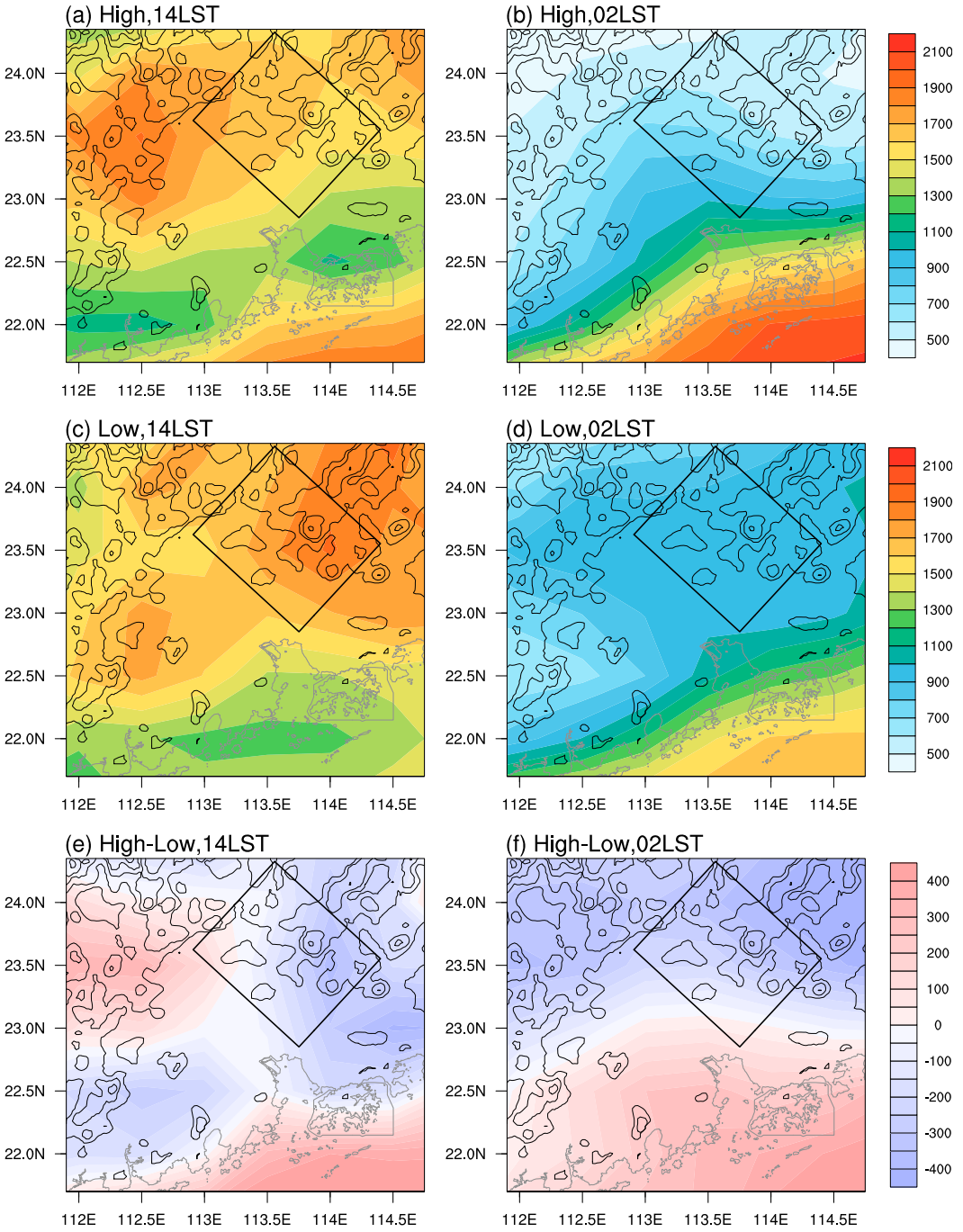

Figure 11. As in Figure 10 but for convection available potential energy (units: J/kg). LST = local standard time.

The 925-hPa mean wind fields (vectors) at 1400 LST and 0200 LST in the high-wind speed (low-wind speed) days are presented in Figures 9a and 9c (Figures 9b and 9d). In general, the mean prevailing low-level winds are southwesterly to southerly with the much stronger wind speed over ocean than that over land. Mean wind speed over PRD in the high-wind speed days is around 7 (8) m/s at 1400 LST (0200 LST). In the low-wind speed days, mean wind speed over PRD is about 1.5 m/s at 1400 LST and 3.5 m/s at nighttime (0200 LST), suggesting that the prevailing wind speed is considerably increased at nighttime in the low-wind speed days. The nighttime acceleration of low-level winds can be seen more clearly by plotting the perturbation wind at 0200 LST (Figures 9e and 9f), the daily mean at 925 hPa has been removed to highlight the

nighttime enhancement. It is shown that nighttime enhancement of low-level wind speed over PRD in the high-wind speed days is around 0.75 m/s (Figure 9e), only reaching 10% of the daily mean wind speed (8 m/s) at 925 hPa. The deviated winds over PRD attains ~1.25 m/s at 0200 LST in the low-wind speed days (Figure 9f), implying that the nocturnal acceleration of the low-level prevailing winds reaches approximately 40% of the daily mean wind speed (3.3 m/s) at 925 hPa.

To further investigate the diurnal variations of low-level winds, the perturbation wind fields at cross sections along the dashed line A-B (southwest-northeast orientation) in Figure 5a at 0800, 1400, 2000, and 0200 LST are shown in Figure 12. The average prevailing winds below 800 hPa over PRD are southwesterly to southerly (not shown). From daytime to nighttime, the horizontal southwesterly wind speeds (shading) over the plains and mountain slopes (22.5–23.5°N) are enhanced from surface to 900 hPa with strongest acceleration occurring at 925 hPa (~1.2 m/s), leading to the strengthened windward dynamic lifting (arrows between 23.2°N and 24°N) in the low-wind speed days (Figure 12h). Consequently, CON increases and results in the early morning peak in the low-wind speed days. However, in the high-wind speed days, the nocturnal acceleration of the prevailing low-level southwesterly winds is weaker (only ~0.5 m/s) and are found at higher levels (above 950 hPa; Figure 12d). The horizontal southwesterly wind speeds decrease with the magnitude up to 1.0 m/s below 975 hPa at 0200 LST. The low-level southwesterly winds are enhanced below 975 hPa at 0800 LST (Figure 12a), indicating that the nocturnal southwesterly winds can also be enhanced but later than that of the low-wind speed days. As a result, the time that CON reaches a local maximum (~0500 LST) under the high-wind speed conditions is 2–3 hr later than the morning peak in the low-wind speed days (~0300 LST; Figure 6a). The horizontal southwesterly wind speeds and windward lifting weaken from surface to 900 hPa in the low-wind speed days at 1400 LST (Figure 12f). However, in the high-wind speed days, the intensified horizontal southwesterly winds below 975 hPa leads to strengthened windward mechanical lifting effect in the afternoon.

The close relationship between the nighttime low-level southwesterly jet in the boundary layer and convection over South China has been well recognized in previous studies (X. Chen et al., 2015; Du & Chen, 2018, 2019), in which the nocturnal boundary layer jet can be mainly attributed to the inertial oscillation (Blackadar, 1957). According to the inertial oscillation theory, the amplitude of nighttime acceleration is proportional to the diurnally varying turbulent mixing and frictional effect in the boundary layer (Blackadar, 1957; Du & Rotunno, 2014). Figure 13 shows the diurnal variations of the GFS planetary boundary layer height (HPBL hereafter) over PRD region. The HPBL is about 1,100–1,300 m along the line A-B in the early afternoon (1400 LST) during the high-wind speed days (Figure 13a). In the low-wind speed days (Figure 13c), the HPBL is higher (1,200–1,500 m) with a local maximum (about 1,500 m) located over the urban area where the surface temperature is highest (Figure 9b). Such difference can be seen more directly by comparing the HPBL difference between different wind speeds days (Figure 13e). Generally, in the low-wind speed days, the HPBL over the northeastern inland mountainous region and adjacent urban area is about 200 m higher than that in the high-wind speed days (Figure 13e). At nighttime, however, the HPBL along the line A-B in the low-wind speed days is 50–150 m lower when compared to that in the high-wind speed days (Figure 13f), especially in the urban area and the windward slope of the northeastern inland mountainous region (100–150 m lower). The larger day-night difference in the HPBL suggests that the diurnal variations of turbulent mixing and frictional effect is stronger in the low-wind speed days, which produces a stronger nocturnal enhancement of the low-level prevailing southwesterly winds (Figure 12h). The increase (reduction) of southwesterly wind speeds below 975 hPa at 1400 (0200) LST is likely due to the sea (land) breeze is established earlier and advected far inland owing to the strong prevailing ambient winds in the high-wind speed days (X. Chen et al., 2017; Hu & Xue, 2016). However, to understand the specific mechanisms responsible for the differences in the diurnal variations of low-level winds under different wind speeds, more studies are required in the future.

5.3. Impacts of Moisture Content in Boundary Layer

X. Chen et al. (2017) suggested that the coastal rainfall of South China is not only controlled by the ambient onshore wind speed but also sensitive to the incoming moisture especially the moisture content in the boundary layer (0–1 km). The influences of the moisture content transported by the low-level winds on the inland orographic convention under different ambient wind speeds are also investigated here.

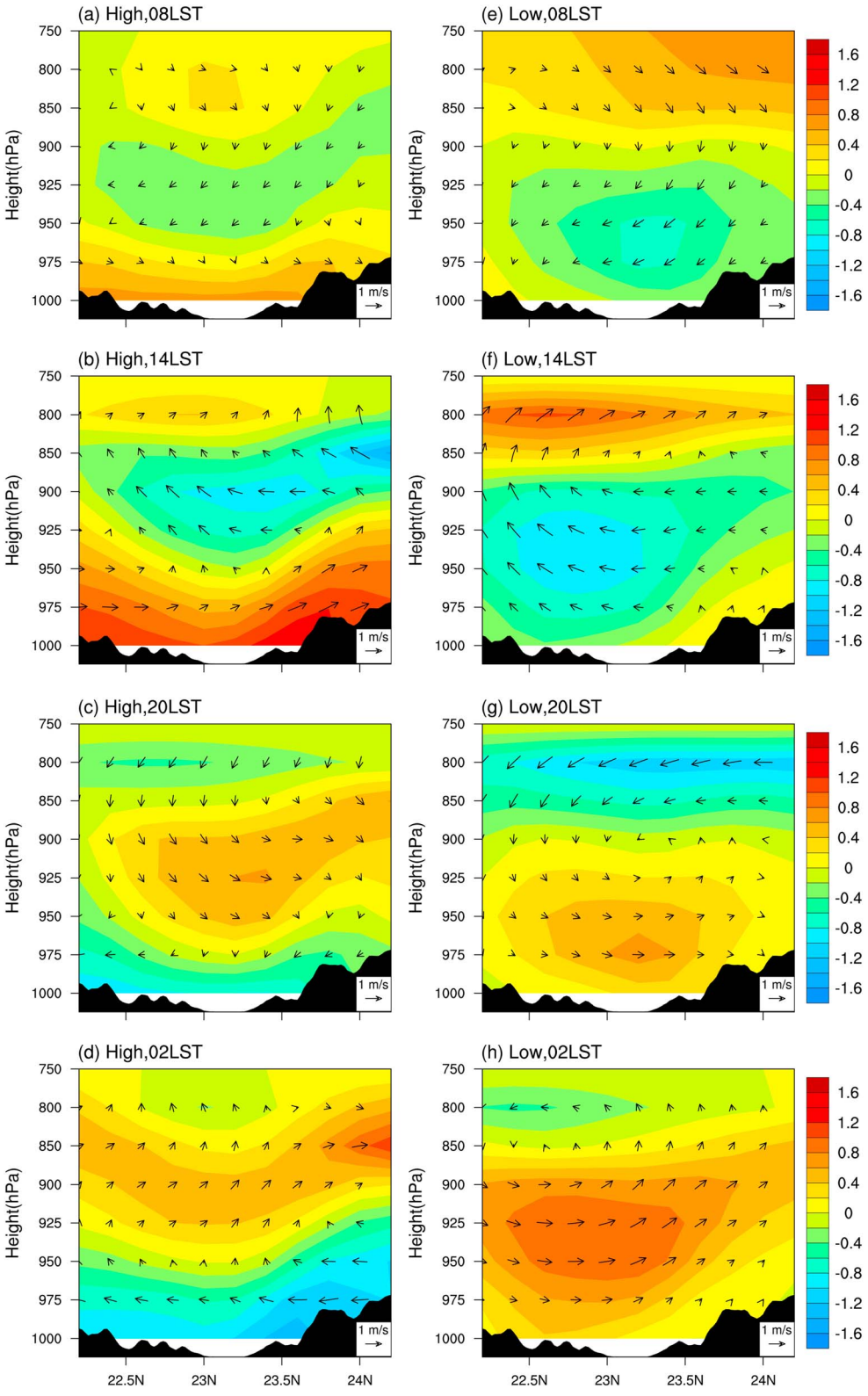

Figure 12. Perturbation wind vectors (arrows) at the cross section along the dashed line A-B in Figure 5a and the perturbation wind component (shading, units: m/s) projected to the plane at (a) 0800 LST, (b) 1400 LST, (c) 2000 LST, and (d) 0200 LST in the high-wind speed days. (e–h) As in (a–d) but for the low-wind speed days. Vertical velocity is scaled by 10 for visualization. Black shading on the bottom of each panel represents the interpolated topographic profiles. LST = local standard time.

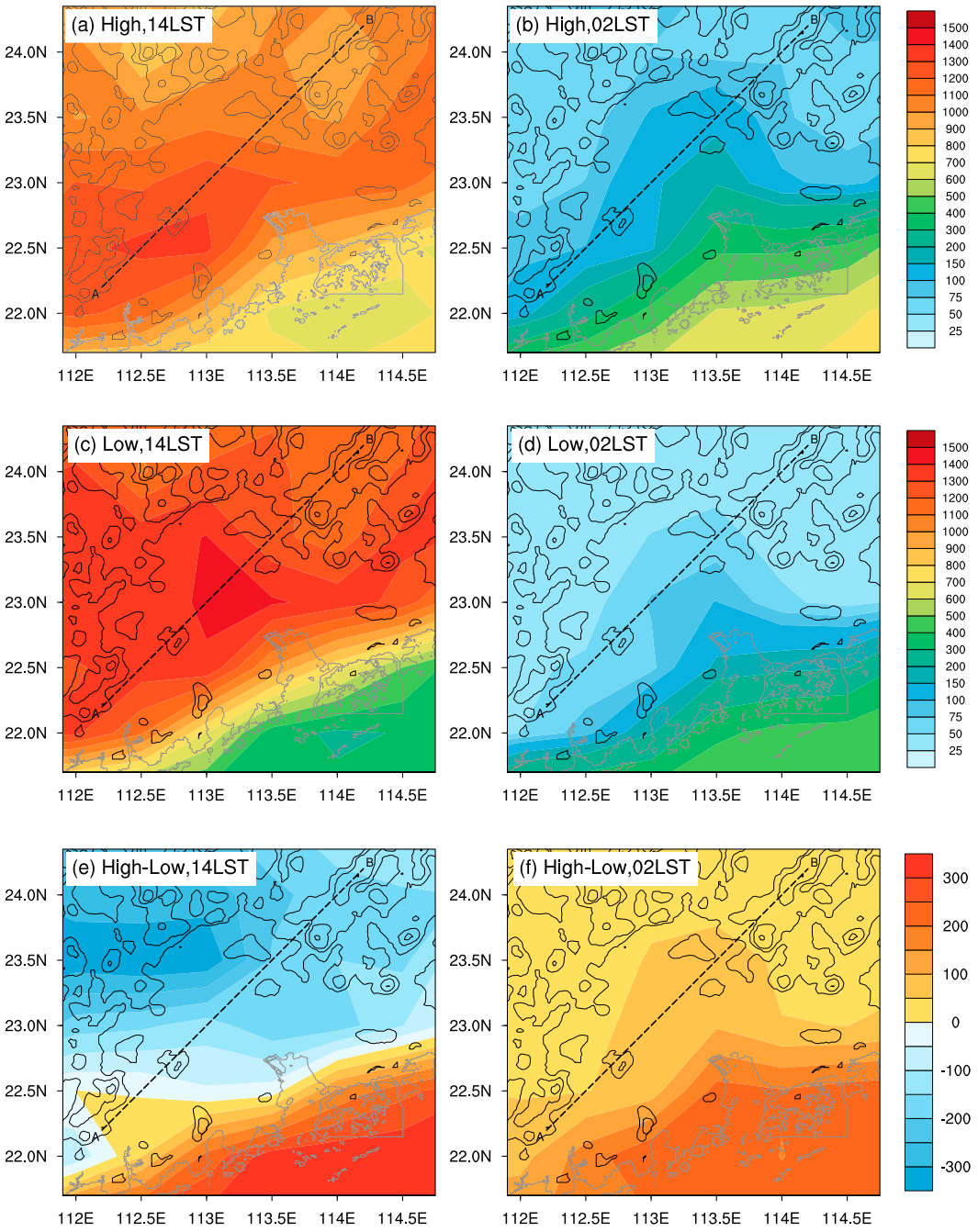

Figure 13. Mean Global Forecast System planetary boundary layer height (units: m) over Pearl River Delta region in the high-wind speed days at (a) 1400 LST and (b) 0200 LST and in the low-wind speed days at (c) 1400 LST and (d) 0200 LST; the planetary boundary layer height of the high-wind speed days minus the low-wind speed days at (e) 1400 LST and (f) 0200 LST. Black contours, from 100 to 1,100 with 200-m intervals, indicate orography. The dashed lines A-B indicate the location of the corresponding vertical cross section presented in Figure 12. LST = local standard time.

First, the daily mean moisture fluxes in the boundary layer in the high-wind speed (Figure 14a) and the low-wind speed days (Figure 14b) are explored. The moisture fluxes is integrated from surface to 900 hPa at each grid and calculated according to Flux $= \frac{1}{g}\int_{p_1}^{p_2} q\vec{V}\,dp$ (g, q, $\vec{V}$, and p are gravity acceleration, specific humidity, the horizontal velocity vector, and pressure, respectively; p_1 and p_2 are respectively the surface pressure and 900 hPa.). Moisture in the boundary layer transported to PRD in the high-wind speed days is more than twice

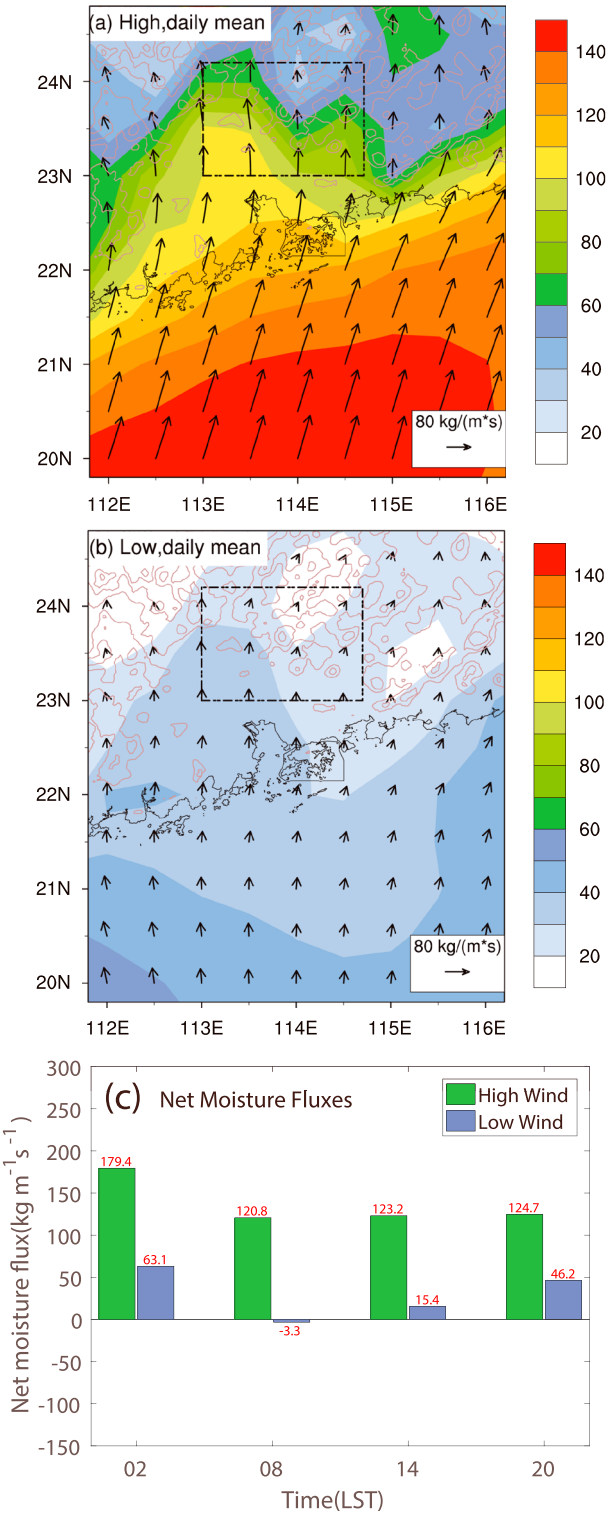

Figure 14. Daily mean water vapor fluxes (units: kg·m^{-1}·s^{-1}) integrated from surface to 900 hPa in (a) the high-wind speed days and (b) the low-wind speed days. (c) Net moisture fluxes (units: kg·m^{-1}·s^{-1}) into the budget region of the inland northeastern mountainous area (22–23°N, 113–114.5°E, indicated by the dashed box in [a, b]) at four times in the high-wind speed and the low-wind speed days. Brown contours in (a, b), from 150 to 1,150 with 250-m intervals, indicate orography. LST = local standard time.

of that in the low-wind speed days (~80 vs. ~30 kg·m^{-1}·s^{-1}), mainly caused by the much stronger low-level prevailing winds.

The diurnal variations of net moisture fluxes into the inland mountainous region (defined as the sum of the moisture fluxes in the four boundaries of dashed boxes in Figures 14a and 14b) are shown in Figure 14c. The net moisture fluxes in the high-wind speed days are higher than that in the low-wind speed days. Especially at 1400 LST, the net moisture fluxes in the high-wind speed days is around 8 times of that in the low-wind speed days (123 vs. 15 kg·m^{-1}·s^{-1}). However, the enhancement of moisture supply from daytime to nighttime in the low-wind speed days is stronger than that in the high-wind speed days as a response to the more significant nighttime enhancement of low-level prevailing winds.

Thus, the early morning peak of CON under the low-wind speed conditions is believed to be due to the enhanced low-level prevailing winds, upslope lifting, and moisture transport. The prevailing wind speeds as well as associated windward lifting effects and moisture transport are much stronger through the whole day in the high-wind speed days, resulting in high CON. In addition, the dominant peak of CON in the afternoon is due to the solar heating, abundant moisture supply, and the enhanced windward mechanical lifting below 975 hPa at 1400 LST. However, the much weaker mechanical windward forcing and net moisture fluxes at 1400 LST result in the remarkable decrease of CON in the afternoon under the low-wind speed conditions.

6. Summary and Conclusions

Complimentary to the previous study of X. Chen et al. (2017) who investigated the influence of monsoonal wind speed and moisture content on the intensity and diurnal variations of coastal rainfall over South China during Mei-Yu season, this study aims to reveal the influence of the low-level monsoonal wind speed on the diurnal variations and intensity of inland orographic convection occurrence frequencies over northeastern PRD, South China, in summer. In this paper, based on 5 years of operational weather radar observations and FNL reanalysis data, the connection between the CON and the synoptic patterns is also examined by utilizing an objective synoptic classification method called the T mode obliquely rotated PCA (PCT method). Main findings are shown as follows:

The climatic mean of the summer time CON and rainfall over PRD, South China, exhibits two maximal centers with one located along the southern coastline region and the other situated over the northeastern mountainous regions. Additionally, about 80% of total summer precipitation are contributed by convective rainfall. The low-level synoptic patterns over South China are classified into nine types with PCT method by using the geopotential height at 925 hPa. Results show that the first two most frequent types (type 1 49% and type 2 17%) account for up to 65%. Prevailing winds over PRD in synoptic pattern of type 1 is close to southwesterly, and the type 2 pattern is featured by stronger southeasterly flows over PRD, South China.

Spatial distributions and diurnal variations of CON and rainfall are closely related to synoptic patterns. The convection and rainfall corresponding to the synoptic pattern of type 1 (2) occur more frequently in the northeastern inland mountains and southern coast (along the southern coastline). The CON on the windward slope corresponding to the type 1 synoptic

pattern exhibits two diurnal peaks with a primary early afternoon peak and a secondary early morning peak. The CON in the synoptic pattern of type 2 also displays similar double peaks. Meanwhile, the convection and rainfall corresponding to type 1 contributes more than 60% of the inland orographic convection and rainfall during summer, indicating that type 1 is the dominant synoptic pattern for the inland orographic convection and rainfall center.

The prevailing low-level wind speed can also affect the intensity and diurnal variations of orographic convection occurrence frequencies in the dominant synoptic pattern of type 1. The CON is much higher in the high-wind speed days than that in the low-wind speed days, especially in the afternoon. The diurnal variation of CON shows a dominant early afternoon peak around 1400 LST and a small increase in the early morning around 0400–0600 LST in the high-wind speed days, while the morning and afternoon peaks of CON become comparable in the low-wind speed days. The convective features are mainly contributed by large and/or deep convective features in the high-wind speed days. In contrast, smaller convection is more likely to occur in the afternoon under the low-wind speed conditions, and the reduction of CON in the afternoon in the low-wind speed days is mainly caused by the decrease of large convection. The convection in the high-wind speed days is mostly concentrated over the windward and mountainous regions and is quasi-stationary. The morning orographic convection in the low-wind speed days exhibits an upstream propagation. This can be partly explained by the cold pool effect, pressure perturbations due to the low-level wind maximum and thermally forced gravity waves.

The terrain thermal effects alone are not strong enough for the orographic convection formation over PRD in summer, and the topography mechanical forcing plays an important role as well. Compared with the high-wind speed days, the much warmer surface over the inland regions leads to much larger land-sea thermal contrast in the low-wind speed days at 1400 LST. In addition, the afternoon CAPE in the high-wind speed days is slightly smaller than that of the low-wind speed days, suggesting that the high CON in the high-wind speed days is not only determined by the thermal environment conditions and the mechanical forcing induced by topography is very important. Relative to the low-wind speed days, the moisture fluxes below 900 hPa are much stronger throughout the whole day in the high-wind speed days. The net moisture fluxes over the inland mountainous region at 1400 LST is about 8 times of that in the low-wind speed days. Under the high-wind speed conditions, the combination of the strong orographic mechanical lifting and the abundant moisture supply leads to high CON, especially the large and/or deep convective features. Diurnal variation of the low-level prevailing winds associated with the inertial oscillation leads to the nocturnal acceleration and daytime deceleration of prevailing winds below 900 hPa under the low-wind speed conditions. Consequently, the prevailing southerly winds and windward mechanical lifting are strengthened at nighttime, resulting in the early morning peak of CON in the low-wind speed days. Under the low-wind speed conditions, afternoon convection (especially the large convective features) are reduced considerably, which can be attributed to the weakened windward dynamic lifting effect and moisture transport as well as more isolated convective features owing to the relative weak ambient wind speeds in the afternoon. In addition, due to the weak dynamical lifting in the afternoon under the low-wind speed conditions, convection is mainly driven by thermal forcing and takes more time to accumulated unstable energy. As a result, the afternoon peak of CON is 2–3 hr later than that in the high-wind speed days. In the high-wind speed days, the nighttime enhancement of prevailing winds below 975 hPa is later than that of the low-wind speed days, and the local maximum of CON in the early morning is 2–3 hr later than the early morning peak of the low-wind speed days. The prevailing winds below 975 hPa is influenced by the sea (land) breeze at 1400 (0200) LST in the high-wind speed days, which may be explained as the sea (land) breeze is established earlier and spread far inland under the high-wind speed conditions.

To understand the mechanism related to the diurnal variations of low-level winds under different ambient wind speeds and the physical link between the prevailing wind speed and the diurnal patterns of inland orographic convection, more studies based on data set with higher resolution as well as convection-permitting numerical sensitivity experiments are required in the future.

Acknowledgments
We gratefully acknowledge Wen-Chau Lee from National Center for Atmospheric Research, Boulder, CO, USA; Chuntao Liu from Texas A&M University; and Yali Luo from Chinese Academy of Meteorological Sciences for their valuable suggestions. We also thank the editor and three reviewers for their comments that improved our paper. This work was primarily supported by the National Key Research and Development Program of China (Grant 2017YFC1501703) and the National Natural Science Foundation of China (Grants 41475015, 41275031, and 41322032), and the Open Research Program of the State Key Laboratory of Severe Weather. We acknowledge Guangdong Meteorological Bureau for collecting and archiving the radar data. The radar data and reanalysis data (FNL and GFS) are available at this website: https://pan.baidu.com/s/1DwaeJepGH0KHmkMa7vjN0w#list/path=%2F.

References

Benedetto, J. J. (1996). *Harmonic analysis and applications*, (Vol. 23). CRC Press, Boca Raton.

Blackadar, A. K. (1957). Boundary layer wind maxima and their significance for the growth of nocturnal inversions. *Bulletin of the American Meteorological Society*, *38*(5), 283–290. https://doi.org/10.1175/1520-0477-38.5.283

Chen, G., Lan, R., Zeng, W., Pan, H., & Li, W. (2018). Diurnal variations of rainfall in surface and satellite observations at the monsoon coast (South China). *Journal of Climate*, *31*(5), 1703–1724. https://doi.org/10.1175/JCLI-D-17-0373.1

Chen, G., Sha, W., & Iwasaki, T. (2009). Diurnal variation of precipitation over southeastern China: 2. Impact of the diurnal monsoon variability. *Journal of Geophysical Research*, *114*, D21105. https://doi.org/10.1029/2009JD012181

Chen, G., Sha, W., Sawada, M., & Iwasaki, T. (2013). Influence of summer monsoon diurnal cycle on moisture transport and precipitation over eastern China. *Journal of Geophysical Research: Atmospheres*, *118*, 3163–3177. https://doi.org/10.1002/jgrd.50337

Chen, M., Wang, Y., Gao, F., & Xiao, X. (2014). Diurnal evolution and distribution of warm-season convective storms in different prevailing wind regimes over contiguous North China. *Journal of Geophysical Research: Atmospheres*, *119*, 2742–2763. https://doi.org/10.1002/2013JD021145

Chen, X., Zhang, F., & Ruppert, J. H. Jr. (2019). Modulations of the diurnal cycle of coastal rainfall over South China caused by the boreal summer intraseasonal oscillation. *Journal of Climate*, *32*(7), 2089–2108. https://doi.org/10.1175/JCLI-D-18-0786.1

Chen, X., Zhang, F., & Zhao, K. (2016). Diurnal variations of the land–sea breeze and its related precipitation over South China. *Journal of the Atmospheric Sciences*, *73*(12), 4793–4815. https://doi.org/10.1175/JAS-D-16-0106.1

Chen, X., Zhang, F., & Zhao, K. (2017). Influence of monsoonal wind speed and moisture content on intensity and diurnal variations of the Mei-Yu season coastal rainfall over South China. *Journal of the Atmospheric Sciences*, *74*(9), 2835–2856. https://doi.org/10.1175/JAS-D-17-0081.1

Chen, X., Zhao, K., & Xue, M. (2014). Spatial and temporal characteristics of warm season convection over Pearl River Delta region, China, based on 3 years of operational radar data. *Journal of Geophysical Research: Atmospheres*, *119*, 12,447–412,465. https://doi.org/10.1002/2014JD021965

Chen, X., Zhao, K., Xue, M., Zhou, B., Huang, X., & Xu, W. (2015). Radar-observed diurnal cycle and propagation of convection over the Pearl River Delta during Mei-Yu season. *Journal of Geophysical Research: Atmospheres*, *120*, 12,557–12,575. https://doi.org/10.1002/2015JD023872

Compagnucci, R. H., & Richman, M. B. (2008). Can principal component analysis provide atmospheric circulation or teleconnection patterns? *International Journal of Climatology: A Journal of the Royal Meteorological Society*, *28*(6), 703–726. https://doi.org/10.1002/joc.1574

Crum, T. D., Alberty, R. L., & Burgess, D. W. (1993). Recording, archiving, and using WSR-88D data. *Bulletin of the American Meteorological Society*, *74*(4), 645–653. https://doi.org/10.1175/1520-0477(1993)074<0645:RAAUWD>2.0.CO;2

Dai, A. (2001). Global precipitation and thunderstorm frequencies. Part II: Diurnal variations. *Journal of Climate*, *14*(6), 1092–1111. https://doi.org/10.1175/1520-0442(2001)014<1092:GPATFP>2.0.CO;2

Du, Y., & Chen, G. (2018). Heavy rainfall associated with double low-level jets over Southern China. Part I: Ensemble-based analysis. *Monthly Weather Review*, *146*(11), 3827–3844. https://doi.org/10.1175/MWR-D-18-0101.1

Du, Y., & Chen, G. (2019). Heavy rainfall associated with double low-level jets over Southern China. Part II: Convection initiation. *Monthly Weather Review*, *147*(2), 543–565. https://doi.org/10.1175/MWR-D-18-0102.1

Du, Y., & Rotunno, R. (2014). A simple analytical model of the nocturnal low-level jet over the Great Plains of the United States. *Journal of the Atmospheric Sciences*, *71*(10), 3674–3683. https://doi.org/10.1175/JAS-D-14-0060.1

Du, Y., & Rotunno, R. (2015). Thermally driven diurnally periodic wind signals off the east coast of China. *Journal of the Atmospheric Sciences*, *72*(7), 2806–2821. https://doi.org/10.1175/JAS-D-14-0339.1

Du, Y., & Rotunno, R. (2018). Diurnal cycle of rainfall and winds near the South Coast of China. *Journal of the Atmospheric Sciences*, *75*(6), 2065–2082. https://doi.org/10.1175/JAS-D-17-0397.1

Hu, X.-M., & Xue, M. (2016). Influence of synoptic sea-breeze fronts on the urban heat island intensity in Dallas–Fort Worth, Texas. *Monthly Weather Review*, *144*(4), 1487–1507. https://doi.org/10.1175/MWR-D-15-0201.1

Huth, R. (1996a). An intercomparison of computer-assisted circulation classification methods. *International Journal of Climatology: A Journal of the Royal Meteorological Society*, *16*(8), 893–922. https://doi.org/10.1002/(SICI)1097-0088(199608)16:8<893::AID-JOC51>3.0.CO;2-Q

Huth, R. (1996b). Properties of the circulation classification scheme based on the rotated principal component analysis. *Meteorology and Atmospheric Physics*, *59*(3), 217–233. https://doi.org/10.1007/BF01030145

Huth, R., Beck, C., Philipp, A., Demuzere, M., Ustrnul, Z., Cahy nová, M., et al. (2008). Classifications of Atmospheric Circulation Patterns. *Annals of the New York Academy of Sciences*, *1146*(1), 105–152. https://doi.org/10.1196/annals.1446.019

Jiang, Z., Zhang, D.-L., Xia, R., & Qian, T. (2017). Diurnal variations of presummer rainfall over Southern China. *Journal of Climate*, *30*(2), 755–773. https://doi.org/10.1175/JCLI-D-15-0666.1

Li, M., Zhang, Q., & Zhang, F. (2016). Hail day frequency trends and associated atmospheric circulation patterns over China during 1960–2012. *Journal of Climate*, *29*(19), 7027–7044. https://doi.org/10.1175/JCLI-D-15-0500.1

Luo, Y., Wang, H., Zhang, R., Qian, W., & Luo, Z. (2013). Comparison of Rainfall Characteristics and Convective Properties of Monsoon Precipitation Systems over South China and the Yangtze and Huai River Basin. *Journal of Climate*, *26*(1), 110–132. https://doi.org/10.1175/JCLI-D-12-00100.1

Luo, Y., Zhang, R., Wan, Q., Wang, B., Wong, W. K., Hu, Z., et al. (2017). The Southern China Monsoon Rainfall Experiment (SCMREX). *Bulletin of the American Meteorological Society*, *98*(5), 999–1013. https://doi.org/10.1175/BAMS-D-15-00235.1

Marshall, J. S., & Palmer, W. M. K. (1948). The distribution of raindrops with size. *Journal of Meteorology*, *5*(4), 165–166. https://doi.org/10.1175/1520-0469%281948%29005%3C0165%3ATDORWS%3E2.0.CO%3B2

Miglietta, M. M., & Rotunno, R. (2009). Numerical simulations of conditionally unstable flows over a Mountain Ridge. *Journal of the Atmospheric Sciences*, *66*(7), 1865–1885. https://doi.org/10.1175/2009JAS2902.1

Mohr, C. G., & Vaughan, R. L. (1979). An economical procedure for Cartesian interpolation and display of reflectivity factor data in three-dimensional space. *Journal of Applied Meteorology*, *18*(5), 661–670. https://doi.org/10.1175/1520-0450(1979)018<0661:AEPFCI>2.0.CO;2

Nugent, A. D., Smith, R. B., & Minder, J. R. (2014). Wind speed control of tropical orographic convection. *Journal of the Atmospheric Sciences*, *71*(7), 2695–2712. https://doi.org/10.1175/JAS-D-13-0399.1

Philipp, A., Beck, C., Huth, R., & Jacobeit, J. (2016). Development and comparison of circulation type classifications using the COST 733 dataset and software. *International Journal of Climatology*, *36*(7), 2673–2691. https://doi.org/10.1002/joc.3920

Richman, M. B. (1986). Rotation of principal components. *Journal of Climatology*, *6*(3), 293–335. https://doi.org/10.1002/joc.3370060305

Romatschke, U., Medina, S., & House, R. A. Jr. (2010). Regional, seasonal, and diurnal variations of extreme convection in the South Asian region. *Journal of Climate*, *23*(2), 419–439. https://doi.org/10.1175/2009JCLI3140.1

Smith, R. B., Minder, J. R., Nugent, A. D., Storelvmo, T., Kirshbaum, D. J., Warren, R., et al. (2012). Orographic precipitation in the tropics: The Dominica Experiment. *Bulletin of the American Meteorological Society*, *93*(10), 1567–1579. https://doi.org/10.1175/BAMS-D-11-00194.1

Sobel, A. H., Burleyson, C. D., & Yuter, S. E. (2011). Rain on small tropical islands. *Journal of Geophysical Research*, *116*, D08102. https://doi.org/10.1029/2010JD014695

Steiner, M., Houze, R. A., & Yuter, S. E. (1995). Climatological characterization of three-dimensional storm structure from operational radar and rain gauge data. *Journal of Applied Meteorology*, *34*(9), 1978–2007. https://doi.org/10.1175/1520-0450(1995)034<1978:CCOTDS>2.0.CO;2

Tian, W.-S., & Parker, D. J. (2002). Two-dimensional simulation of orographic effects on mesoscale boundary-layer convection. *Quarterly Journal of the Royal Meteorological Society*, *128*(584), 1929–1952. https://doi.org/10.1256/003590002320603476

Wallace, J. M. (1975). Diurnal variations in precipitation and thunderstorm frequency over the conterminous United States. *Monthly Weather Review*, *103*(5), 406–419. https://doi.org/10.1175/1520-0493%281975%29103%3C0406%3ADVIPAT%3E2.0.CO%3B2

Wang, C. C., Kuo, H. C., Johnson, R. H., Lee, C. Y., Huang, S. Y., & Chen, Y. H. (2015). A numerical study of convection in rainbands of Typhoon Morakot (2009) with extreme rainfall: Roles of pressure perturbations with low-level wind maxima. *Atmospheric Chemistry and Physics*, *15*(19), 8479–8523.

Wang, H., Luo, Y., & Jou, B. J.-D. (2014). Initiation, maintenance, and properties of convection in an extreme rainfall event during SCMREX: Observational analysis. *Journal of Geophysical Research: Atmospheres*, *119*, 13,206–213,232. https://doi.org/10.1002/2014JD022339

Wang, S., & Sobel, A. H. (2017). Factors controlling rain on small tropical islands: Diurnal cycle, large-scale wind speed, and topography. *Journal of the Atmospheric Sciences*, *74*(11), 3515–3532. https://doi.org/10.1175/JAS-D-16-0344.1

Wu, Y., Huang, A., Huang, D., Chen, F., Yang, B., Zhou, Y., et al. (2018). Diurnal variations of summer precipitation over the regions east to Tibetan Plateau. *Climate Dynamics*, *51*(11), 4287–4307. https://doi.org/10.1007/s00382-017-4042-x

Xu, W., & Zipser, E. J. (2011). Diurnal variations of precipitation, deep convection, and lightning over and East of the Eastern Tibetan Plateau. *Journal of Climate*, *24*(2), 448–465. https://doi.org/10.1175/2010JCLI3719.1

Xu, W., & Zipser, E. J. (2012). Properties of deep convection in tropical continental, monsoon, and oceanic rainfall regimes. *Geophysical Research Letters*, *39*, L07802. https://doi.org/10.1029/2012GL051242

Yin, S., Chen, D., & Xie, Y. (2009). Diurnal variations of precipitation during the warm season over China. *International Journal of Climatology*, *29*(8), 1154–1170. https://doi.org/10.1002/joc.1758

Yuan, W., Yu, R., Chen, H., Li, J., & Zhang, M. (2010). Subseasonal characteristics of diurnal variation in summer monsoon rainfall over Central Eastern China. *Journal of Climate*, *23*(24), 6684–6695. https://doi.org/10.1175/2010JCLI3805.1

Zhang, C.-Z., Uyeda, H., Yamada, H., Geng, B., & Ni, Y. (2006). Characteristics of mesoscale convective systems over the east part of continental China during the Meiyu from 2001 to 2003. *Journal of the Meteorological Society of Japan, Series II*, *84*(4), 763–782.

Zhang, J., Wang, S., & Clarke, B. (2004). P5. 4 WSR-88D reflectivity quality control using horizontal and vertical reflectivity structure. Paper presented at the Proceedings of the llth Conference on Aviation, Range and Aerospace Meteorology. IS.

Zhou, T., Yu, R., Chen, H., Dai, A., & Pan, Y. (2008). Summer precipitation frequency, intensity, and diurnal cycle over China: A comparison of satellite data with rain gauge observations. *Journal of Climate*, *21*(16), 3997–4010. https://doi.org/10.1175/2008JCLI2028.1